



**HAL**  
open science

# Benchmark of identification methods for the estimation of building wall thermal resistance using active method: Numerical study for IWI and single-wall structures

Thanh-Tung Ha, Vincent Feuillet, Julien Waeytens, Kamel Zibouche, Simon Thebault, Rémi Bouchie, Véronique Le Sant, Laurent Ibos

## ► To cite this version:

Thanh-Tung Ha, Vincent Feuillet, Julien Waeytens, Kamel Zibouche, Simon Thebault, et al.. Benchmark of identification methods for the estimation of building wall thermal resistance using active method: Numerical study for IWI and single-wall structures. *Energy and Buildings*, 2020, 224, pp.110130. 10.1016/j.enbuild.2020.110130 . hal-03021973

**HAL Id: hal-03021973**

**<https://hal.science/hal-03021973>**

Submitted on 22 Aug 2022

**HAL** is a multi-disciplinary open access archive for the deposit and dissemination of scientific research documents, whether they are published or not. The documents may come from teaching and research institutions in France or abroad, or from public or private research centers.

L'archive ouverte pluridisciplinaire **HAL**, est destinée au dépôt et à la diffusion de documents scientifiques de niveau recherche, publiés ou non, émanant des établissements d'enseignement et de recherche français ou étrangers, des laboratoires publics ou privés.



Distributed under a Creative Commons Attribution - NonCommercial 4.0 International License

1 **Benchmark of identification methods for the estimation of building wall**  
2 **thermal resistance using active method: numerical study for IWI and single-**  
3 **wall structures**

4 Thanh-Tung HA<sup>a</sup>, Vincent FEUILLET<sup>a\*</sup>, Julien WAEYTENS<sup>b</sup>, Kamel ZIBOUCHE<sup>c</sup>,  
5 Simon THEBAULT<sup>c</sup>, Rémi BOUCHIE<sup>c</sup>, Véronique LE SANT<sup>d</sup>, Laurent IBOS<sup>a</sup>

6 <sup>a</sup> *Univ Paris Est Creteil, CERTES, F-94010 Creteil, France*

7 <sup>b</sup> *Univ Gustave Eiffel, IFSTTAR, Cité Descartes, 14-20 Boulevard Newton, 77420 Champs-sur-*  
8 *Marne, France*

9 <sup>c</sup> *Centre Scientifique et Technique du Bâtiment (CSTB), 84 Avenue Jean Jaurès, 77420 Champs-*  
10 *sur-Marne, France*

11 <sup>d</sup> *Laboratoire National de Métrologie et d'Essais (LNE), 29 Rue Roger Hennequin, 78197 Trappes,*  
12 *France*

13  
14 <sup>\*</sup> *corresponding author: [vincent.feuillet@u-pec.fr](mailto:vincent.feuillet@u-pec.fr); phone: +33 (0)1 45 17 18 43; fax: +33 (0)1 45*  
15 *17 65 51*

16

17 **Abstract:**

18 The determination of the thermal resistance of a building envelope is fundamental for the  
19 evaluation of the thermal performance of buildings. This could help to evaluate and verify  
20 the energy efficiency performance of constructions before renovation, during construction,  
21 upon delivery and during use. Some methods exist in the scientific literature but they do not  
22 allow a systematic, accurate and rapid evaluation. This paper presents a numerical  
23 benchmark of identification methods used to estimate the thermal resistance of an opaque  
24 wall. The robustness of each identification technique is investigated in terms of bias and

25 uncertainties. The proposed estimation approach is based on an active method, in which the  
26 structure is heated in order to create a temperature gradient across the wall, and on the  
27 analysis in dynamic regime of the thermal response of the wall. The investigated walls are  
28 internal wall insulation (IWI) and single-wall structures (SWS). The results of the  
29 numerical study show that RC model-based identification techniques are the most suitable  
30 to estimate the thermal resistance of IWI at a very low computational cost. Nevertheless,  
31 the modelling error being larger for the SWS than for the IWI, 1D transient heat equations  
32 should be preferred for the identification of SWS thermal resistance. The active thermal  
33 strategy allows a relevant estimation of the thermal resistance with an observation time of  
34 less than 24 h.

35

36 **Keywords:**

37 Building envelope; Thermal resistance; Numerical benchmark; Active method;  
38 Identification.

39

40 **Highlights:**

- 41 - Assessment of the thermal resistance of opaque building walls
- 42 - Comparison of identification methods within the scope of a numerical benchmark
- 43 - Analysis of the bias and uncertainties of the inverse methods
- 44 - Influence of the wall structure, time observation, outdoor conditions and wall  
45 orientation

## 46 1. Introduction

47 Thermal insulation of buildings is a key factor to guarantee the thermal comfort of the  
48 occupants and to achieve high energy savings. Nowadays the number of uninsulated or  
49 insufficiently insulated existing buildings remains quite significant in France. A massive  
50 renovation operation is needed in order to upgrade the energy performance of these  
51 buildings. The thermal transmittance ( $U$ -value) of a building wall, closely related to the  
52 thermal resistance, can represent its thermal insulation quality. The consumption objectives  
53 imposed by the RT2012 in France [1] result in a minimum resistance value of about 4  
54  $\text{m}^2\cdot\text{K}\cdot\text{W}^{-1}$  for an opaque building wall. It is important to notice that these requirements will  
55 continue to increase in future regulations. Against this background, it is essential to be able  
56 to assess building wall thermal performance before the renovation, during construction,  
57 upon delivery, and during use. This would require undertaking an *in situ* measurement.

58 On the whole building level, methods already exist for identifying the overall thermal  
59 performance of the envelope. *In situ* evaluation of a building overall insulation has been a  
60 subject addressed in European projects [2] as well as by international research groups in  
61 Annex 58 of the IEA [3]. Currently, two approaches have been proposed in the literature to  
62 evaluate the overall performance of the envelope:

- 63 - identification methods based on indirect measurements used in occupied buildings  
64 and on modelling of the building in varying levels of detail: simple thermal balance  
65 [4], RC modelling with statistical analysis for the stochastic grey-box model [5];

66 - measurement methods in controlled heating conditions in unoccupied buildings,  
67 avoiding sunlight crossing windowed walls: co-heating method [3], ISABELLE  
68 transient state method [6] or Quick U-Building (QUB) method [7].

69 The proposed paper concerns the thermal diagnosis at the wall scale. An article  
70 presented recently a review of the different passive measurement methods for obtaining the  
71 thermal transmittance of various elements of a house [8]: heat flow meter, guarded hot  
72 plate, guarded hot box and infrared thermography technique (IRT). Results of laboratory  
73 and *in situ* are under review. Quantitative IRT is considered as the most active area of  
74 research for building analysis but the influence of environment and surface characteristics  
75 should be quantified. Moreover, the authors show that IRT can be used as a support for  
76 other techniques in case of non-homogeneous structures. The determination of the thermal  
77 resistance of a wall (or of the *U*-value) is the subject of two standardized methods, both  
78 based on the analysis of a stationary thermal regime. ISO 8990 [9] uses a guarded hot box  
79 facility and requires one to four days of experimentation in laboratory, depending on wall  
80 thermal inertia, in particular to achieve steady conditions on both sides of the wall. This  
81 standard gives a stability criterion on temperatures: the temporal variation shall be less than  
82 1% of the average temperature difference between hot and cold environments. ISO 9869-1  
83 [10] relies on the heat flow meter method. It is an *in situ* direct method based on the  
84 measurement of mean values for internal heat flux and internal and external surface  
85 temperatures. However, it requires a measurement time greater than 3 days, stable  
86 meteorological conditions and a high temperature gradient across the wall. In addition, this  
87 standard indicates a significant measurement uncertainty (between 14 and 28% depending  
88 on the type of wall). Several works in literature were derived from the ISO 9869-1

89 standard. Rasooli *et al.* [11] proposed revisiting the standard to reduce the *in situ*  
90 measurement durations by using a method called the “Excitation Pulse Method” (EPM),  
91 based on the theory of thermal response factors [12]. Same authors recently used this  
92 method in [13] to assess several thermo-physical properties of a wall (thermal conductivity,  
93 volumetric heat capacity, thickness) but the authors noted that this method is less efficient  
94 with heavily insulated walls because of lateral effects. Nowoświat *et al.* [14] proposed a  
95 mean computation of  $U$ -value on the whole surface by using internal surface resistance  
96 which is evaluated by approximating the internal surface heat transfer coefficient, so as not  
97 to have to measure the heat flow rate. Depending on the type of wall, a list of correcting  
98 coefficients and disturbed values coming from surrounding conditions and physical  
99 characteristics of tested wall are introduced in order to complete all possible influences in  
100 computing. The obtained results showed absolute error less than 10 % compared to ISO  
101 9869-1 method in all investigated cases. Certain authors focused on the estimation of the  $U$ -  
102 value when climate conditions change suddenly and proposed modifying the method  
103 recommended by the standard by applying moving averages. For this, Naveros *et al.* [15]  
104 used non-linear models that take these various phenomena into account.

105 Other reference measurements are carried out with infrared thermography instead of  
106 contact sensors in the same context of a pseudo-stationary regime. In Danielski *et al.* [16],  
107 the envelope heat transfer coefficient of an external wall was measured thanks to interior  
108 infrared measurements over a period of two weeks and a half and steady-state heat transfer  
109 equations. Albatici *et al.* developed in several references [17,18] another passive  
110 thermographic approach allowing the *in situ* determination of the thermal transmittance of a  
111 wall. The method is based on a steady-state heat balance assuming that the conduction

112 exchange across the wall is equal to the radiation and convection exchange of the wall with  
113 the outside. The measurements are all done from the outside of the building. Nardi *et al.*  
114 [19] used the same infrared approach to measure from outside the thermal transmittance of  
115 a brick wall coated with an insulating layer of polystyrene. Similar work was developed in  
116 [20] but measurements are made from the inside of the building. A similar approach was  
117 used by Tejedor *et al.* [21] to determine *in situ* *U*-values of single-leaf walls and multi-leaf  
118 walls by means of quantitative internal IRT. The experimental set-up included an IR  
119 camera, a reflector, a blackbody, and a thermohygrometer. A temperature difference of 7°C  
120 between indoor and outdoor environments is required and only unoccupied buildings can be  
121 studied to best meet the steady-state hypothesis. The same authors studied in [22] the  
122 influence of operating conditions such as the interior-exterior temperature difference and  
123 the type of wall investigated. Kato *et al.* [23] used passive thermography with additional  
124 elements on the wall, i.e. heat transfer coefficient and environmental temperature sensors.  
125 An extension of ISO-9869-1 is based on this work and has been published recently [24].  
126 This approach consists in observing the inside surface of the wall to be characterized using  
127 an infrared camera and recording a sequence of thermal images for several days (3 to 6  
128 days in the proposed standard).

129 Other works rely on identification methods based on contact measurements with  
130 thermocouples and flow meters or infrared thermography. Sassine [25] proposed an  
131 experimental tool for performing *in situ* measurements on walls based on a two-port  
132 formalism [26]. Authors proposed calculating the theoretical heat flux from *R* and *C* values  
133 in the literature, then using this theoretical curve to calibrate it to that of the experimental  
134 heat flux via ordinary least squares or the gradient descent method (non-linear

135 optimization) [27]. This approach was also used in [28] to determine the thermophysical  
136 properties of a wall using the simplex method. Biddulph *et al.* used a Bayesian estimation  
137 method [29] for simultaneously estimating two thermophysical properties: thermal  
138 resistance and thermal inertial. One of the advantages of this method is that it makes it  
139 possible to perform measurements in a few days since it does not require reaching steady-  
140 state or a minimum difference of 10°C between the interior and exterior temperatures.  
141 Another work [30] proposed the development of a Bayesian approach allowing the  
142 determination of the thermal properties of a wall ( $U$ -value and  $C$ -value) and their associated  
143 uncertainties from measurements of near-air internal and external temperatures and internal  
144 surface heat flux. The data came from a winter measurement campaign in an occupied UK  
145 dwelling over a 14 day period during the winter. The authors considered that a satisfactory  
146 estimate of  $U$  is possible over a period of one day. Petojević *et al.* [31] worked on the  
147 evaluation of the thermal transmittance based on the thermal impulse response (TIR) and  
148 Tikhonov regularization technique. Instead of using classic computations of passive  
149 methods, the authors proposed a numerical model of two inputs-two outputs for the tested  
150 wall by using the surface temperatures and heat fluxes on the internal and external facades  
151 in dynamic conditions. With 105 hours of measurement, this study confirmed the  
152 possibility for predicting the dynamic thermal characteristics, cumulative heat losses, heat  
153 accumulation, conductive part of thermal transmittance and surface heat fluxes. A  
154 measurement protocol of the thermal resistance of an insulated internal wall was  
155 established in [32] by using active infrared thermography. The panels were heated using  
156 halogen spots placed inside a heating reflector and a step heating excitation was used.  
157 Thermal quadrupoles were used to analyze thermogram sequences. An identification

158 method led to the estimation of four parameters including the time constant of the  
159 insulating layer. The feasibility of this method was proven in laboratory for different multi-  
160 layered panels fixed onto a building wall.

161         The present study is a part of the French National Research project named  
162 RESBATI whose main objective is to develop a portable measurement device for  
163 evaluating the thermal resistance of opaque building walls on site. The result of the thermal  
164 resistance measurement should be provided with its uncertainty. The device will be used  
165 not only to assess opaque wall elements after construction, upon delivery of new buildings  
166 or for running diagnostics on existing buildings, but also for self-monitoring on  
167 construction sites. For new buildings, the assessment will enable auto control for building  
168 craftsmen and a guaranty of performance for householders. For existing buildings,  
169 assessment before and after refurbishment will allow estimating gain of performance. The  
170 device ought to be simple to use and of moderate cost so that it may be acquired and used  
171 by craftsmen. The active method is chosen in the project, which is an uncommon approach  
172 in the field of measuring the thermal resistance of a wall. It involves artificially producing a  
173 thermal excitation so as to create a temperature gradient across the wall being studied, and  
174 recording a sequence of temperatures, for instance by using infrared thermography. The  
175 RESBATI project aims to demonstrate the strengths of the active approach: the assessment  
176 should be able to be carried out at any time of year (low influence of meteorological  
177 conditions), for any type of building and use thereof (occupied or otherwise) and for quite  
178 short measurement times (around a few hours).

179         The task "Study of methods robustness" of the RESBATI project aimed to test the  
180 physical models and the identification methods of the project partners (CERTES, CSTB,

181 IFSTTAR, LNE) in the context of a thermal excitation of the wall and the analysis of its  
182 response in dynamic regime. This numerical step consisted in conducting an identification  
183 method benchmark to evaluate the identification capacity of the inverse methods (estimated  
184 value, uncertainty, calculation time) according to the test characteristics (wall type, weather  
185 conditions, duration of the test, etc.). This benchmark was a preliminary step to the sizing  
186 of the prototype currently tested. This article is devoted to the presentation of the main  
187 results of this numerical benchmark. It will focus on the estimation of thermal resistance on  
188 opaque walls of buildings with internal wall insulation (IWI) and single-wall structures  
189 (SWS).

190 The article is organized as follows. After the introduction, the considered approach  
191 for the comparative study of identification methods is outlined. In section 2, the wall test  
192 cases and the different Generating Physical Models (GPM) used to generate the numerical  
193 data set are presented. Then, the identification methods to assess the wall thermal resistance  
194 are described in section 3. Lastly, the results of the identification methods are analysed and  
195 compared in section 4.

196

197 **2. Methods**

198 **2.1 General Methodology**

199 The proposed numerical identification benchmark aims to study the robustness of the  
200 identification methods used, by comparing:

- 201 - the bias of each identification method which is the difference between the thermal  
202 resistance value identified by each method and the exact value;  
203 - the uncertainty on this identified thermal resistance value, which is estimated  
204 differently for each identification protocol.

205 It is crucial to investigate the bias to ensure that the exact value of the thermal  
206 resistance is inside the uncertainty interval predicted by the identification method. If not,  
207 the application field of the identification method should be restricted.

208 However, the bias estimate requires a perfectly known reference thermal resistance  
209 value. For this reason, the benchmark methodology is based on numerical experiments  
210 carried out by Generating Physical Models (GPM), in which the physical inputs for each  
211 material are perfectly controlled (thermal conductivity, thickness, etc.). By simulating an  
212 experiment using these GPMs and identifying the thermal resistance with one of the  
213 identification methods, the identified thermal resistance  $\hat{R}$  can be compared to the exact  
214 value  $\tilde{R}$  derived from the known input parameters used in the GPM. The reliability of the  
215 estimate is therefore verified by carrying out this comparison. It is important to note here  
216 that this work does not involve real measurement data, the identifications are based on data  
217 calculated in the context of numerical experiments. The global benchmark methodology is  
218 described in the following steps:

- 219 - Cross-checking the different Generating Physical Models used by each participant, by  
 220 comparing transient results with well-known analytic solutions of the heat transfer  
 221 equation (this part will not be presented in this article);
- 222 - Describing several realistic test cases: wall components commonly present in French  
 223 buildings, boundary conditions, solicitations, etc. (see section 2.2);
- 224 - At a third step, GPMs are used to generate numerical experiments for each test case.  
 225 The generated data set is then used by each participant in his identification protocol to  
 226 guess the thermal resistance value and estimate the associated uncertainty. A blind  
 227 process is considered (only the wall typology, i.e. IWI or SWS is known before  
 228 conducting the identification). The CERTES was in charge of collecting all exact and  
 229 identified  $R$ -values. The results of the blind process are presented in section 4.

230 The blind process is summed up in figure 1:

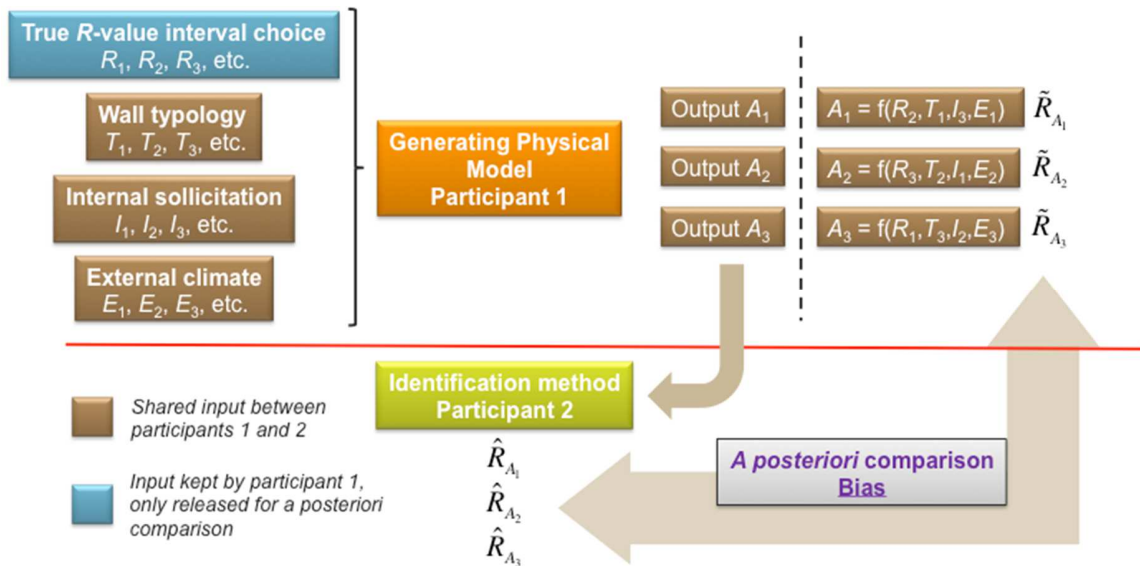


**Fig. 1.** Blind identification of  $R$ -value - benchmark principles.

231 **2.2 Description of the test cases**

232 This part presents the inputs and outputs of the test cases to be implemented in the  
233 GPMs (described in section 2.3).

234 **2.2.1 Wall structures and properties**

235 The numerical benchmark is based on wall components that are common in French  
236 buildings, especially in dwellings. The composition of each layer of the studied wall  
237 typologies, i.e. internal wall insulation (IWI) and single-wall structures (SWS), are  
238 presented in figure 2. The physical properties of each layer (thermal conductivity, heat  
239 capacity, thickness, etc.) have to be chosen by each GPM user into a physical range. The  
240 precise chosen values are not sent to other participants so that they can blindly identify the  
241 thermal resistance. At the end of the blind process only the CERTES knows all the values  
242 in order to make the comparison between exact and identified  $R$ -values possible.

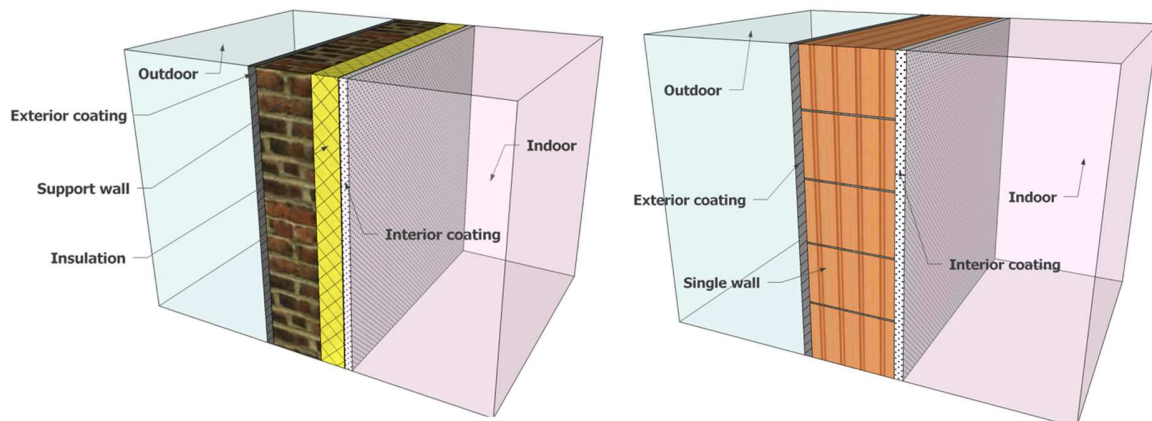


**Fig. 2.** Internal wall insulation (IWI, left) and single-wall structure (SWS, right) considered in the *Generating Physical Models*.

243 Table 1 contains the intervals derived from professional knowledge, for each  
244 parameter and each wall component, in which GPM users could choose one specific value

245 for blind benchmark. These intervals have been constructed for common materials used in  
 246 these kinds of wall components, physical properties are mainly extracted from French  
 247 thermal regulation default values [33]. Note that GPMs consider ideal situations regarding  
 248 the materials constituting the walls. Thus the degradation of the building envelope (joints,  
 249 bricks, etc.) or the effect of moisture are not taken into account in the simulations.

Wall typology	Layer - number	Thickness $e_i$ (m)	Thermal conductivity $\lambda_i$ ( $\text{W}\cdot\text{m}^{-1}\cdot\text{K}^{-1}$ )	Density $\rho_i$ ( $\text{kg}\cdot\text{m}^{-3}$ )	Heat capacity $c_i$ ( $\text{J}\cdot\text{K}^{-1}\cdot\text{kg}^{-1}$ )
IWI	Plasterboard or internal coating - #1	$0.01 \leq e_1 \leq 0.03$	$0.2 \leq \lambda_1 \leq 0.8$	$600 \leq \rho_1 \leq 1500$	1000
	Insulation - #2	$0.04 \leq e_2 \leq 0.2$	$0.02 \leq \lambda_2 \leq 0.06$	$30 \leq \rho_2 \leq 150$	$900 \leq c_2 \leq 1400$
	Support wall - #3	$0.15 \leq e_3 \leq 0.3$	$0.1 \leq \lambda_3 \leq 2.3$	$650 \leq \rho_3 \leq 2500$	1000
	External coating - #4	$0.01 \leq e_4 \leq 0.03$	$0.3 \leq \lambda_4 \leq 1.8$	$500 \leq \rho_4 \leq 2000$	1000
SWS	Plasterboard or internal coating - #1	$0.01 \leq e_1 \leq 0.03$	$0.2 \leq \lambda_1 \leq 0.8$	$600 \leq \rho_1 \leq 1500$	1000
	Single wall - #2	$0.3 \leq e_2 \leq 0.4$	$0.1 \leq \lambda_2 \leq 0.4$	$650 \leq \rho_2 \leq 1200$	1000
	External coating - #3	$0.01 \leq e_3 \leq 0.03$	$0.3 \leq \lambda_3 \leq 1.8$	$500 \leq \rho_3 \leq 2000$	1000

250 **Table 1.** Intervals of possible values for wall physical properties involved in the blind numerical  
 251 benchmark.

### 252 2.2.2 Indoor conditions

253 The active approach planned in the RESBATI project consists in heating a specific  
 254 zone of the internal wall face (distant from openings and thermal bridges in order to study a  
 255 1D heat transfer zone through the wall) with a Heaviside thermal solicitation. A step  
 256 excitation is thus applied on the heating zone in the simulations (figure 3), i.e. the heat flux  
 257  $\Phi_{si}$  applied on the internal wall surface is equal to  $0 \text{ W}\cdot\text{m}^{-2}$  during the first hour of the test,  
 258 then  $400 \text{ W}\cdot\text{m}^{-2}$ . As the estimation of the thermal resistance must be rapid, the duration of

259 the thermal excitation is limited to 24 hours.

260 The experimental prototype planned in the project will heat a 0.6 m by 0.6 m wall  
261 area. The entire section of the wall considered in GPMs is 2 m by 2 m in order to take into  
262 account the 3D effects inevitably encountered in a real measurement situation. The rest of  
263 the wall exchanges with the indoor air by convection and radiation. In all the numerical  
264 experiments, the indoor air temperature  $T_i$  is fixed at 20°C.

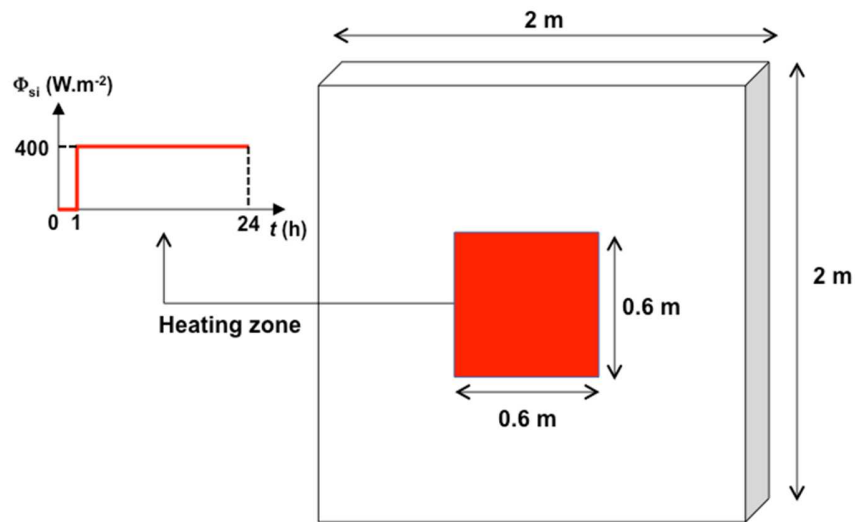


**Fig. 3.** Schematic view of the internal surface of the wall with the heating zone considered in the Generating Physical Models.

### 265 2.2.3 Outdoor conditions

266 Two external climates over a 24-hour period are considered, extracted from the  
267 French thermal regulation inputs [34]:

- 268 - H1a (Trappes): from April the 1<sup>st</sup> at 4 pm to April the 2<sup>nd</sup> at 4 pm, north orientation;
- 269 - H2d (Carpentras): from October the 1<sup>st</sup> at 10 am to October the 2<sup>nd</sup> at 10 am, south  
270 orientation.

271 These two data sets are used to address different weather conditions, times of day, and wall  
 272 orientations. The useful climatic inputs from these climate data sets, available for a time  
 273 step of 5 minutes, are described in table 2.

Input	Unit	Description
$T_e$	°C	External air temperature
$dirN$	W.m <sup>-2</sup>	Direct normal solar radiation
$diff$	W.m <sup>-2</sup>	Diffuse solar radiation
$Gamma$	°	Solar altitude
$Psi$	°	Solar orientation regarding the south direction (negative in the sunrise)

274 **Table 2.** Climatic inputs considered in the Generating Physical Models.

275 The global incident solar radiation  $\Phi_{sol}$  on the vertical wall is obtained using the  
 276 following equations, allowing computing direct, diffuse and reflected incident solar  
 277 radiations on a given wall from climatic data sets [35]:

$$278 \quad \Phi_{sol} = \Phi_{dir} + \Phi_{diff} + \Phi_{ref} \quad (1)$$

$$279 \quad \Phi_{dir} = \text{Max}(0; dirN \times \cos(Gamma) \times \cos(Psi - \alpha_z)) \quad (2)$$

$$280 \quad \Phi_{diff} = \frac{diff}{2} \quad (3)$$

$$281 \quad \Phi_{ref} = \frac{alb}{2} \times (diff + dirN \times \sin(Gamma)) \quad (4)$$

282 with  $\Phi_{dir}$ ,  $\Phi_{diff}$  and  $\Phi_{ref}$  respectively the direct, diffuse and ground reflected incident solar  
 283 radiation on the wall,  $\alpha_z$  the wall orientation regarding the south direction (south = 0°, north  
 284 = 180°) and  $alb$  the environment external albedo, assumed to be zero ( $alb = 0$ ).

285 The solar radiation applied on the external surface of the wall  $\Phi_{se}$  is then:

286 
$$\Phi_{se} = \alpha_e \times \Phi_{sol} \quad (5)$$

287 with  $\alpha_e$  the external solar absorption coefficient, supposed to be equal to 0.6 (medium  
288 color). It should be noted here that longwave radiation with the environment (ground, sky,  
289 other buildings, etc.) and latent effects due to moisture and rain are neglected.

290 Figure 4 shows the two climate data as a function of the observation time  $t$  of the  
291 numerical experiment in terms of external air temperature  $T_e$  and solar radiation applied on  
292 the external surface  $\Phi_{se}$ . Relatively different environmental conditions can be observed: the  
293 external air temperature for the Carpentras climate is significantly higher than in Trappes  
294 and the maximum solar flux occurs at different times of the numerical experiment.

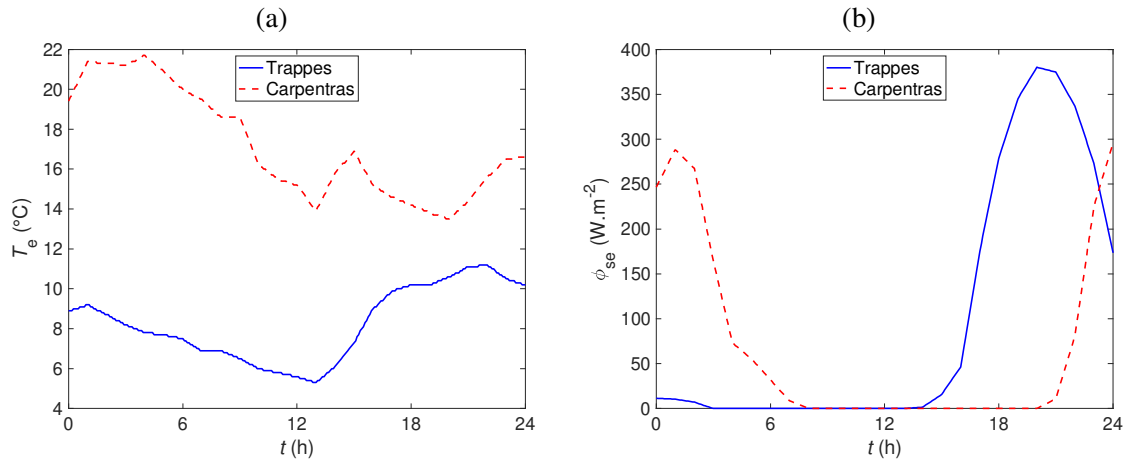


**Fig. 4.** Climate data (Trappes and Carpentras) according to the observation time of the numerical experiment: (a) External air temperature, (b) Solar radiation applied on the external surface.

295 **2.2.4 Initial and boundary conditions**

296 The temperature field inside the wall is initialized by a linear temperature evolution  
297 between the internal and external faces.

298 Boundary conditions are modelled by global indoor and outdoor heat exchange  
299 coefficients, taking both convection and radiation into account (see table 3). These  
300 conventional values are extracted from the French thermal regulation inputs, referring to  
301 [36].

<b>Environment</b>	<b>Global heat exchange coefficients <math>h</math> (convection + radiation) (<math>\text{W.m}^{-2}.\text{K}^{-1}</math>)</b>
Indoor	7.7
Outdoor	25

302 **Table 3.** Global heat exchange coefficients considered in the Generating Physical Models.

### 303 **2.2.5 Data set considered in the Generating Physical Models**

304 In addition to indoor and outdoor conditions described previously, a numerical  
305 experiment data set is calculated using GPMs to be used as inputs for identification  
306 methods. These computed data include the evolutions of the internal and external wall  
307 surface temperatures ( $T_{si}$  and  $T_{se}$ ) and of the heat flux absorbed by heat conduction by the  
308 internal wall surface ( $\Phi_{abs}$ ), and are taken at the center of the heating zone shown in figure  
309 3. This data set is presented as time series with 30 seconds time step. Depending on the  
310 identification method, it may be resampled before applying the identification protocol.  
311 Figure 5 and table 4 describe all the data generated in the data set.

312

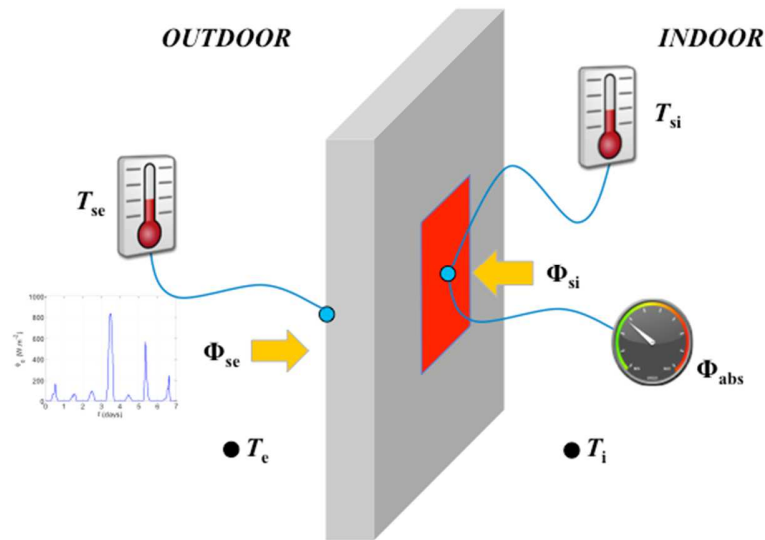


Fig. 5. Locations of data generated in the numerical experiments carried out by Generating Physical Models.

Environment	Data	Notation	Unit
Indoor	Internal air temperature	$T_i$	$^{\circ}\text{C}$
	Internal wall surface temperature*	$T_{si}$	$^{\circ}\text{C}$
	Heat flux applied on the heating zone	$\Phi_{si}$	$\text{W}\cdot\text{m}^{-2}$
	Heat flux absorbed in the wall*	$\Phi_{abs}$	$\text{W}\cdot\text{m}^{-2}$
Outdoor	External air temperature	$T_e$	$^{\circ}\text{C}$
	External wall surface temperature*	$T_{se}$	$^{\circ}\text{C}$
	Solar radiation applied on the external surface	$\Phi_{se}$	$\text{W}\cdot\text{m}^{-2}$

313 **Table 4.** Data set generated in the numerical experiments and used as inputs for identification  
 314 methods (\*: data computed by the Generating Physical Model).

315 After being generated, a realistic measurement noise is added on each computed  
 316 temperature and heat flux data, in order to evaluate the robustness of each identification  
 317 method (originally designed for noisy data sets from real measurements). These noises are

318 obtained experimentally on thermocouples and fluxmetric plates of characteristics similar  
319 to those planned in the experimental prototype and were recorded for 72 hours. The noisy  
320 data set is then the same for each participant.

## 321 **2.3 Generating Physical Models**

322 The Generating Physical Models are used to generate numerical experiments which  
323 provide data to be analyzed by each identification method (see section 3) to estimate the  
324 thermal resistance of the wall. All GPMs are 3D in order to take into account the transverse  
325 heat transfers occurring in the wall in a real measurement situation. Let us remind that a  
326 cross-check of each GPM has been performed in a preliminary stage to compare the  
327 numerical outputs to known analytical solutions. Each GPM (partners involved: CERTES,  
328 CSTB and LNE) is shortly described in the following sections.

### 329 **2.3.1 CERTES: Thermal quadrupole simulations**

330 A semi-analytic model using the thermal quadrupole method has been developed as  
331 GPM (3D QUAD) by CERTES. This method is based on Laplace transform and integral  
332 transforms (for multidimensional simulations) of the theoretical heat transfer equation to  
333 represent the transient thermal state of a multilayer wall by a matrix relation [37].

334 Let us first consider a simple homogeneous wall of isotropic material which has  
335 limited size ( $L_x \times L_y \times e$ ) and whose thermal conductivity and thermal diffusivity are noted  
336 respectively  $\lambda$  and  $a$ . By using Laplace transform on time variable and Fourier transform in  
337 space (see equation (7)), we can simplify 3D transient heat transfer equation by:

$$338 \quad \frac{\partial^2 \hat{\theta}}{\partial z^2}(\alpha_n, \beta_m, z, p) = \left(\frac{p}{a} + \alpha_n^2 + \beta_m^2\right) \hat{\theta}(\alpha_n, \beta_m, z, p) = \gamma^2 \hat{\theta}(\alpha_n, \beta_m, z, p) \quad (6)$$

339 with:

340 
$$\hat{\theta}(\alpha_n, \beta_m, z, p) = \int_0^\infty \int_0^{L_x} \int_0^{L_y} T(x, y, z, t) U(\alpha_n, x) V(\beta_m, y) e^{-pt} dx dy dt \quad (7)$$

341 where  $U(\alpha_n, x)$  and  $V(\beta_m, y)$  are the eigenfunctions corresponding to eigenvalues  $\alpha_n$  and  $\beta_m$   
 342 respectively. The expressions of these eigenfunctions depend on boundary conditions  
 343 according to [37]. In this study, because of adiabatic condition on the boundaries, cosine  
 344 and sinus functions are chosen for  $U(\alpha_n, x)$  and  $V(\beta_m, y)$ :  $U(\alpha_n, x) = \cos(\alpha_n x)$  and  
 345  $V(\beta_m, y) = \sin(\beta_m y)$ . Finally, we can write down a relation of thermal states of two sides of  
 346 our considered wall using a matrix  $M$ , which is called quadrupole transfer matrix:

347 
$$\begin{pmatrix} \hat{\theta}(\alpha_n, \beta_m, 0, p) \\ \hat{\phi}(\alpha_n, \beta_m, 0, p) \end{pmatrix} = \begin{pmatrix} ch(e\gamma) & (\lambda\gamma)^{-1} sh(e\gamma) \\ \lambda\gamma sh(e\gamma) & ch(e\gamma) \end{pmatrix} \begin{pmatrix} \hat{\theta}(\alpha_n, \beta_m, e, p) \\ \hat{\phi}(\alpha_n, \beta_m, e, p) \end{pmatrix} = M \begin{pmatrix} \hat{\theta}(\alpha_n, \beta_m, e, p) \\ \hat{\phi}(\alpha_n, \beta_m, e, p) \end{pmatrix} \quad (8)$$

348 with  $\gamma = \sqrt{p/a + \alpha_n^2 + \beta_m^2}$ . The advantage of quadrupole computation is the linearity of  
 349 matrix calculation. If we have a wall of  $n$  layers of different materials, the global transfer  
 350 matrix of whole wall is the product of all individual transfer matrices.

351 However, the solution obtained is transformed, so several inverse transforms are used  
 352 to bring this solution back to spatial and temporal spaces. The spatial integral transform is  
 353 based on expansion of Fourier series of a function, so the inverse of this transform is only  
 354 the direct Fourier expansion. For Laplace transform, there are several different approaches  
 355 for inverse transform, theoretically or numerically. After an efficiency comparison, the  
 356 numerical inversion of de Hoog [38] was chosen as the inverse of Laplace transform  
 357 because of its accuracy and rapidity in computation.

358 In addition, external influences such as air temperature, solar radiation or thermal  
 359 excitation of the internal wall surface, which are also considered in quadrupole computation  
 360 need to be transformed in Laplace and Fourier spaces. However, they are measured data

361 which are hardly expressed by a simple analytic function. Therefore, a discrete Laplace  
362 transform is applied for these inputs by applying the principle of superposition of linear  
363 function transforms. In the case of the thermal excitation which is applied on a limited  
364 surface of the internal wall, we fit the spatial form of excitation by a polynomial then  
365 calculate theoretically its Fourier transform.

### 366 **2.3.2 CSTB: VOLTRA simulations**

367 The CSTB used VOLTRA<sup>®</sup> software which is a thermal analysis program, developed  
368 by Physibel<sup>®</sup> for transient heat transfer in three-dimensional rectangular objects [39]. The  
369 time-dependent boundary conditions are described with functions, either built-in functions  
370 based on parameters, or external user-functions based on values given at a fixed time  
371 interval. Dynamic solar heat gains can be studied using a solar processor. An object image  
372 with shadows cast by direct sunlight at any time and any geographic location can be  
373 viewed. The direct and diffuse solar radiation from climate data is cast on the material  
374 surfaces. The absorbed solar radiation is converted to time dependent node powers, as  
375 additional boundary conditions to the system.

376 VOLTRA allows creating time-dependent graphic animations of moving shadow  
377 patterns, calculated temperature and heat flux fields in the studied object. Alphanumeric  
378 lists of time functions of temperatures in individual nodes or heat flow through given  
379 surfaces through the object can be made.

380 The transient heat conduction through solid layers is calculated using a semi-implicit  
381 finite difference method. Air layers are modelled by an equivalent solid layer, estimated a  
382 global thermal conductivity including convection and radiation as described in [36].

383 Concerning boundaries, two options are available: define global heat exchange transfer  
384 coefficients  $h_i$  and  $h_e$ , including convection and radiation or separate heat transfer  
385 coefficients between convection ( $h_{ci}$  and  $h_{ce}$ ) and radiation (calculated using emissivities of  
386 surfaces and radiant temperatures).

387 Two experimental validations of the program VOLTRA for simulating 3D transient  
388 heat transfer were done using an insulated test box with one transparent side [40]. The  
389 simulated temperatures were compared to thermocouple measurements (box surface and air  
390 temperatures). The first was carried out under indoor controlled laboratory conditions by  
391 investigating the transient heat transfer due to a sudden internal power source. In the  
392 second, the experiment box was put in outdoor conditions to validate the solar processor  
393 module in VOLTRA. These experimental validations were conducted in the framework of  
394 the SBO project IWT 050154 research program “Heat, air and moisture performance  
395 engineering. A whole building approach” [41]. Results showed that the software  
396 reproduced correctly thermal phenomena such as 2D/3D conduction, solar absorption,  
397 infrared radiation and air temperature gradient. Overall the correspondence between  
398 measured and simulated temperatures was quite good for the two experiments. The biggest  
399 deviations were less than 10 % and could be explained by a simplified empirical convection  
400 model and the inaccuracy of some of the boundary conditions.

### 401 **2.3.3 LNE: COMSOL simulations**

402 A numerical model using the COMSOL Multiphysics® software [42] has been  
403 developed by the LNE to study heat transfer in multi-layer walls. The 3D time-dependent  
404 problem is solved using finite element method in space and backward differential formula

405 in time. The algorithm used to solve the system of linear equations is the iterative solver  
 406 GMRES (generalized minimum residual method). Concerning the spatial discretization, the  
 407 mesh of tetrahedral elements is automatically adapted according to a mesh quality criterion.  
 408 Illustrations of the mesh quality and of an internal wall surface temperature are given in  
 409 figure 6. Concerning the time discretization, a fixed time stepping of 30 s is considered.

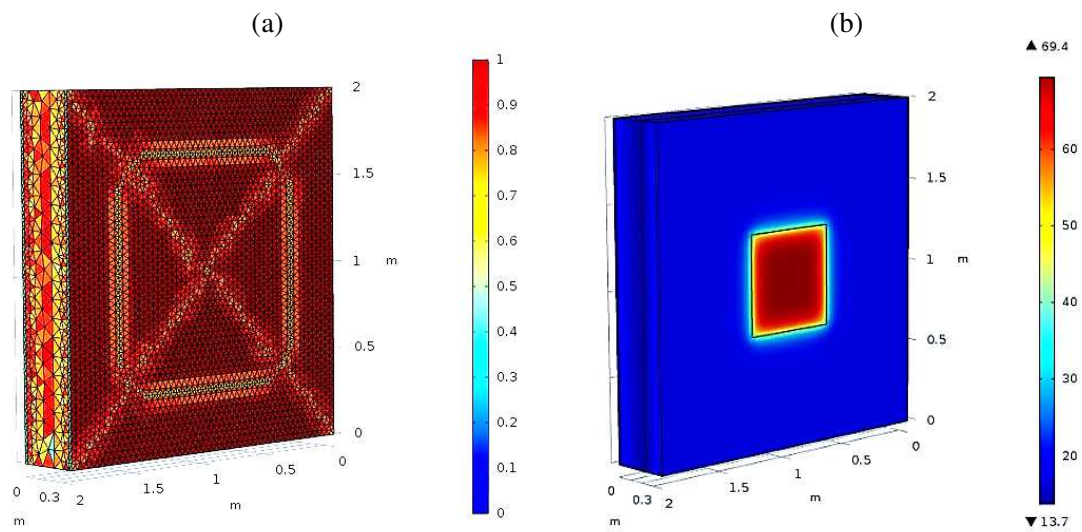


*Fig. 6. Example of COMSOL simulation: (a) Mesh quality, (b) Internal wall surface temperature.*

410 For example, for an IWI wall consisting of 4 layers: external coating (0.02 m thick),  
 411 support wall (0.22 m thick), insulation (0.12 m thick) and internal coating (0.02 m thick),  
 412 the complete mesh consists of 107170 tetrahedral elements which represents about 64000  
 413 degrees of freedom.

#### 414 **2.4 Summary of test cases generated in the numerical benchmark**

415 The numerical benchmark of identification methods involves 26 test cases of IWI and  
 416 SWS walls. Eighteen cases of IWI were generated: 4 walls by CERTES with two different  
 417 climates, 5 walls by CSTB, and 5 walls by LNE. These cases are numbered from 1 to 18.

418 Eight cases of SWS were generated: 2 walls by CERTES for two different climates, 2 walls  
419 by CSTB, and 2 walls by LNE. They are numbered from 19 to 26. Table 5 details the test  
420 cases generated by each GPM user. The corresponding wall thermal resistances are  
421 calculated from the material properties of the wall layers chosen by GPM modeller in table  
422 1 and will serve as exact values  $\tilde{R}$  for the estimates carried out by the identification  
423 methods.

Test case	Benchmark participant	Generating Physical Model	Wall typology	External climate	Wall orientation	Thermal resistance (m <sup>2</sup> .K.W <sup>-1</sup> )	
1	CERTES	3D QUAD	IWI	H2d (Carpentras)	South	2.75	
2						3.52	
3						3.58	
4						3.90	
5				H1a (Trappes)	North	2.75	
6						3.52	
7						3.58	
8						3.90	
9	CSTB	VOLTRA		H1a (Trappes)	North	0.92	
10				H2d (Carpentras)	South	2.34	
11						4.72	
12				H1a (Trappes)	North	5.66	
13	8.62						
14	LNE	COMSOL		H1a (Trappes)	North	1.15	
15						3.23	
16						3.52	
17			3.58				
18	8.37						
19	CERTES	3D QUAD	SWS		H2d (Carpentras)	South	1.05
20							1.05
21	H1a (Trappes)	North			1.05		
22				1.05			
23	CSTB	VOLTRA	H1a (Trappes)	North	1.53		
24					3.34		
25	LNE	COMSOL	H1a (Trappes)	North	1.05		
26					3.08		

424 **Table 5.** List of the test cases generated in the numerical benchmark of identification methods.

425

426 **3. Identification methods**

427 This section is devoted to the detailed presentation of the identification methods  
 428 investigated in the numerical benchmark (partners involved: CERTES, CSTB and  
 429 IFSTTAR).

430 **3.1 CERTES: thermal quadrupoles and Bayesian estimation**

431 An identification method, based on Bayesian approach by using the 1D thermal  
 432 quadrupoles (1D QUAD) as direct model, has been developed by CERTES. With the same  
 433 expression as equation (8), direct model has only one dimension, then  $\gamma = \sqrt{p/a}$  and only  
 434 Laplace transform is in use. Because a lot of compositions of wall properties can lead to the  
 435 same temperature evolution, searching in multidimensional space of parameters seems  
 436 costly and less robust, so a fixed thickness is defined for each layer according to each type  
 437 of wall (see table 6) and the identification process tries to estimate thermal conductivity  $\lambda$   
 438 and product of density with specific heat capacity  $\rho c$ . The total thickness of the wall  $e_{tot}$  is  
 439 fixed at a realistic value (0.4 m) and is not estimated in the identification process.

IWI			SWS		
Layer number	Layer	Thickness $e_i$ (m)	Layer number	Layer	Thickness $e_i$ (m)
#1	Internal coating	0.01	#1	Internal coating	0.01
#2	Insulation layer	$0.4 \times (e_{tot} - 0.02)$	#2	Support wall	$e_{tot} - 0.02$
#3	Support wall	$0.6 \cdot (e_{tot} - 0.02)$	#3	External coating	0.01
#4	External coating	0.01			

440 **Table 6.** Layer thicknesses for IWI and SWS ( $e_{tot}$  is the total thickness) considered in CERTES  
 441 identification process.

442 Following a sensitivity test for the two types of wall, the temperature on the external  
443 surface  $T_{se}$  shows a weak sensitivity related to the parameters of the two first layers in IWI  
444 case which are the willing targets to estimate. On the contrary, the temperature on the  
445 internal surface  $T_{si}$  presents a high value of sensitivity coefficient in both IWI and SWS  
446 cases. Therefore,  $T_{si}$  was chosen as minimization parameter. Bayesian inference is the core  
447 algorithm of the identification method. With the random walk of each parameter, we can  
448 draw a distribution (or Markov chain) of this parameter following direct model and  
449 measured minimization parameter. The most popular method of generating this random  
450 chain is Metropolis-Hasting [43,44]. For optimizing Markov chain generator, Vihola [45]  
451 proposed a new alternative to the Metropolis-Hastings approach called Robust Adaptive  
452 Metropolis (RAM). This algorithm uses a matrix factor  $S$  that captures the shape of the  
453 target distribution and at the same time allows reaching a given mean acceptance rate. The  
454 RAM process can be presented in 5 steps:

- 455 - **Step 1:** Defining a proposal density  $q$  which is spherically symmetric, a  $\mathbb{R}^{d \times d}$  positive  
456 lower-diagonal matrix  $S_1$ , a step size sequence decaying to zero  $\{\eta_n\}_{n \geq 1} \subset (0,1]$ , the  
457 target distribution  $\pi$ , the initial point  $X_1 \in \mathbb{R}^d$  and the target mean acceptance  
458 probability of the algorithm  $\alpha_*$ .
- 459 - **Step 2:** In  $n^{\text{th}}$  iteration, computing  $Y_n := X_{n-1} + S_{n-1}U_n$ , where  $U_n \sim q$ .
- 460 - **Step 3:** Computing the probability  $\alpha_n := \min\{1, \pi(Y_n)/\pi(X_{n-1})\}$ , if the proposal is  
461 accepted,  $X_n = Y_n$ . Otherwise,  $X_n = X_{n-1}$ .
- 462 - **Step 4:** Computing the positive lower-diagonal matrix  $S_n$  which satisfying:

$$463 \quad S_n S_n^T = S_{n-1} (I_d + \eta_n (\alpha_n - \alpha_*) \frac{U_n U_n^T}{\|U_n\|^2}) S_{n-1}^T$$

464 where  $I_d \in \mathbb{R}^{d \times d}$  stands for the identity matrix.

465 - **Step 5:** Returning to step 2 with  $(n + 1)^{\text{th}}$  iteration.

466 Figure 7 presents step-by-step the identification process. Starting with a set of initial  
 467 values of physical parameters (noted  $\lambda_{i\text{-ini}}$  and  $(\rho c)_{i\text{-ini}}$  for  $i^{\text{th}}$  layer), normalized parameters  
 468  $A$  whose initial values are fixed at 1 are considered as estimated parameters to avoid the  
 469 mismatch of parameter magnitude during estimation. For each set of measurement data, a  
 470 Markov chain is generated by proposed algorithm, then a nearly Gaussian histogram based  
 471 on this chain is obtained for each estimated parameter, and mean value and standard  
 472 deviation can be determined. The final values of  $\lambda_i$  and  $(\rho c)_i$  will be calculated from these  
 473 values and initial values at the beginning, then the thermal resistance  $R$  and its uncertainty  
 474 will be determined by the two final equations in figure 7. If we have new data set (for  
 475 instance next hour of measurement), the initial values of normalized parameters for the next  
 476 process will be replaced by estimation results of the previous data set. This replacement  
 477 allows limiting seeking zone of Markov chain generation so that computation time can  
 478 become less costly.

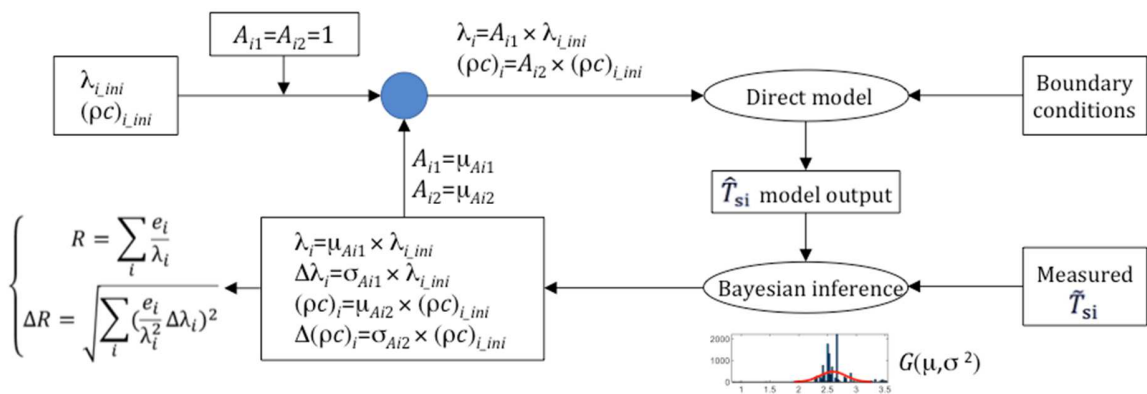


Fig. 7. Overview of the identification process used by CERTES.

479 **3.2 CSTB: RC networks and ISABELE method**

480 In the CSTB approach (based on the ISABELE method [6]), the thermal behavior of  
 481 the wall is modelled by a variety of RC networks (all structures are detailed in Appendix  
 482 A). The corresponding differential equations are converted into stochastic state-space  
 483 models (of orders 1 to 3). These are simulated to estimate the internal wall surface  
 484 temperature  $T_{si}$ . The resistances, capacities, initial temperature of the nodes, and model  
 485 error standard deviations are then adjusted by means of an optimization algorithm to  
 486 maximize the following likelihood function:

$$487 \quad L(\theta, T_{si}) = \prod_{k=t_1}^{t_n} \frac{e^{-0.5\epsilon_k^T R_k^{-1} \epsilon_k}}{\sqrt{\det(S_k)}(\sqrt{2\pi})^l} \quad (9)$$

488 where  $k$  is the 1-dimensional prediction error, with corresponding covariance matrix  $S_k$ ,  
 489 which is calculated by means of a Kalman filter.

490 All this procedure can be done using the CTSM-R package [46]. The most suitable  
 491 model is then selected by using likelihood ratio tests [5,6]. The estimated  $R$ -value of the  
 492 wall corresponds to the equivalent resistance between the internal and external surface  
 493 nodes. Its uncertainty can be computed by using the direct formula:

$$494 \quad \hat{\sigma}_{R_{wall}} = \sqrt{Jcov(\hat{R}_k)J^T} \quad (10)$$

495 where  $J$  corresponds to the Jacobian of the  $R_{wall}$  function (depending on the RC structure)  
 496 and  $cov(\hat{R}_k)$  to the covariance matrix of the estimated resistances, that is obtained by using  
 497 Bayesian inversion. In a nutshell, the principle is to decompose the likelihood profile of the  
 498 optimum (Hessian  $H_\theta$ ) by a set of finite-difference derivatives and to decompose its inverse  
 499 into the following form:

$$500 \quad H_\theta^{-1} = \sigma_\theta^T G \sigma_\theta \quad (11)$$

501 where  $\sigma_\theta$  is the diagonal matrix of the fitted parameters standard deviations and  $G$  the  
 502 corresponding matrix of correlation. It is assumed that all parameters uncertainties are  
 503 Gaussian. More details can be found in the CTSM manual [47].

### 504 **3.3 IFSTTAR: 1D finite element method and gradient descent algorithm with** 505 **adjoint state**

506 In the IFSTTAR approach, the thermal behavior of the wall is modelled by one-  
 507 dimensional (1D) transient heat equations considering 4 layers (resp. 3 layers) for the IWI  
 508 (resp. SWS). The system of partial differential equations is solved in a standard way using a  
 509 finite element method in space and an Euler implicit time integration scheme. Concerning  
 510 the wall identification, nor the thickness nor the thermal properties are known. To  
 511 circumvent the inverse problem be ill-posed, we only identify the thermal conductivity and  
 512 the specific heat capacity of each layer. The layer thicknesses are fixed to mean values  
 513 derived from physical variation ranges given in table 1. The considered thicknesses of the  
 514 layers are summarized in table 7. In summary, the strategy consists of identifying the  
 515 overall thermal resistance of the wall by setting the thickness layers and updating the  
 516 thermal conductivities.

IWI			SWS		
Layer number	Layer	Thickness $e_i$ (m)	Layer number	Layer	Thickness $e_i$ (m)
#1	Internal coating	0.02	#1	Internal coating	0.02
#2	Insulation layer	0.12	#2	Support wall	0.35
#3	Support wall	0.22	#3	External coating	0.02
#4	External coating	0.02			

517 **Table 7.** Layer thicknesses for IWI and SWS considered in IFSTTAR identification process.

518 The IFSTTAR inverse problem, presented in figure 8, reads as follows: “the model  
 519 parameters are sought such that it minimizes a datamisfit functional including a Tikhonov  
 520 regularization term [48]”. We consider the internal and external wall surface temperatures  
 521 in the identification process. The minimization problem is solved using a gradient descent  
 522 algorithm where the functional gradient is estimated at a low computational cost using the  
 523 adjoint state. The model updating process stops when the parameter modifications between  
 524 two successive iterations are less than 0.1 %.

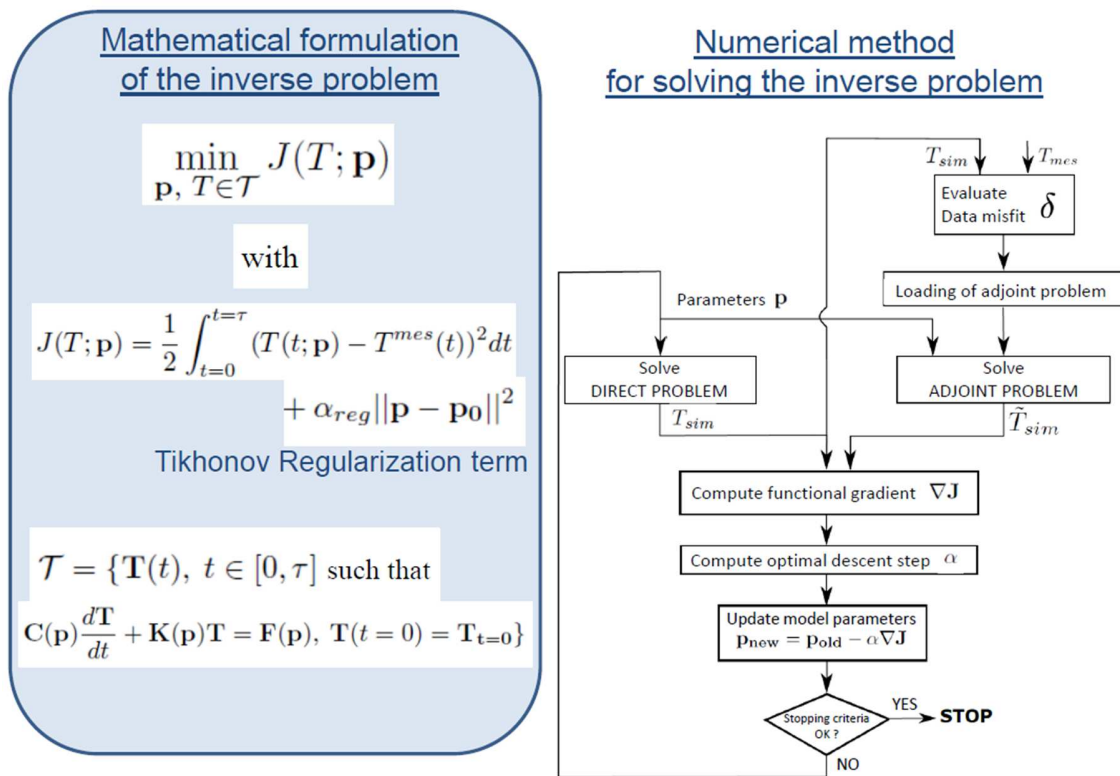


*Fig. 8. Overview of the identification process used by IFSTTAR.*

525 Let us note that the scaling regularization parameter  $\alpha_{reg}$ , involved in the functional  $J$   
 526 in figure 8, is chosen according to L-curve method [49] while ensuring an extended  
 527 discrepancy principle taking into account both measurement and model errors. Hence, at

528 the end of the model updating process the data misfit has to be closed and strictly higher  
 529 than the data misfit threshold defined by:

$$530 \quad J_s = \frac{1}{2} \left\{ \int_{t=0}^{t=t_f} (\varepsilon_{meas,ei}^2 + \varepsilon_{mod,ei}^2) dt + \int_{t=0}^{t=t_f} (\varepsilon_{meas,ee}^2 + \varepsilon_{mod,ee}^2) dt \right\} \quad (12)$$

531 where  $\varepsilon_{meas,ei}$  (resp.  $\varepsilon_{meas,ee}$ ) denotes the measurement error of the temperature sensor at the  
 532 internal wall surface (resp. at the external wall surface) provided by the numerical  
 533 experiments and  $\varepsilon_{mod,ei}$  (resp.  $\varepsilon_{mod,ee}$ ) denotes the model error at the internal wall surface  
 534 (resp. at the external wall surface). Herein, the model error comes from the simplification  
 535 of the 3D transient heat problem by 1D transient heat equations. The estimation of the  
 536 model errors for IWI and SWS is detailed in Appendix B.

537 The inverse technique provides a deterministic estimation of the model parameters.  
 538 A confidence interval on the identified thermal resistance is derived from the calculations  
 539 and the plots of functional iso-values according to the two most sensitive model parameters,  
 540 i.e. the thermal conductivities of the insulation and the support wall for IWI (resp. the  
 541 thermal conductivity and the specific heat capacity of the single-wall layer for SWS). For  
 542 example, we present in figure 9 the iso-values of the data misfit functional for IWI case #15  
 543 considering a 12 h time observation, as a function of the dimensionless thermal  
 544 conductivities of the insulation and the support wall. These dimensionless values, noted  
 545 with a bar in figure 9, are defined as the ratio of the thermal conductivity and the initial  
 546 guess of the thermal conductivity ( $0.04 \text{ W.m}^{-1}.\text{K}^{-1}$  for the insulation layer and  
 547  $1.2 \text{ W.m}^{-1}.\text{K}^{-1}$  for the support wall of the IWI). The model parameters identified by the  
 548 deterministic IFSTTAR inverse approach are represented using a black cross. In this case,  
 549 the data misfit functional at the end of the model updating process is  $1.06 \times 10^3 \text{ }^\circ\text{C}^2.\text{s}$ , which

550 is closed but strictly higher than the modelling error threshold determined in table B.1.  
 551 Herein, let us note that the measurement error is negligible as regards to the modelling  
 552 error. Lastly, from the iso-value contour at  $1.06 \times 10^3 \text{ }^\circ\text{C}^2 \cdot \text{s}$ , the minimum and the maximum  
 553 values of the insulation thermal conductivity  $\lambda_2$  and the support wall thermal conductivity  
 554  $\lambda_3$  are obtained, which allow estimating a confidence interval on the wall thermal  
 555 resistance.

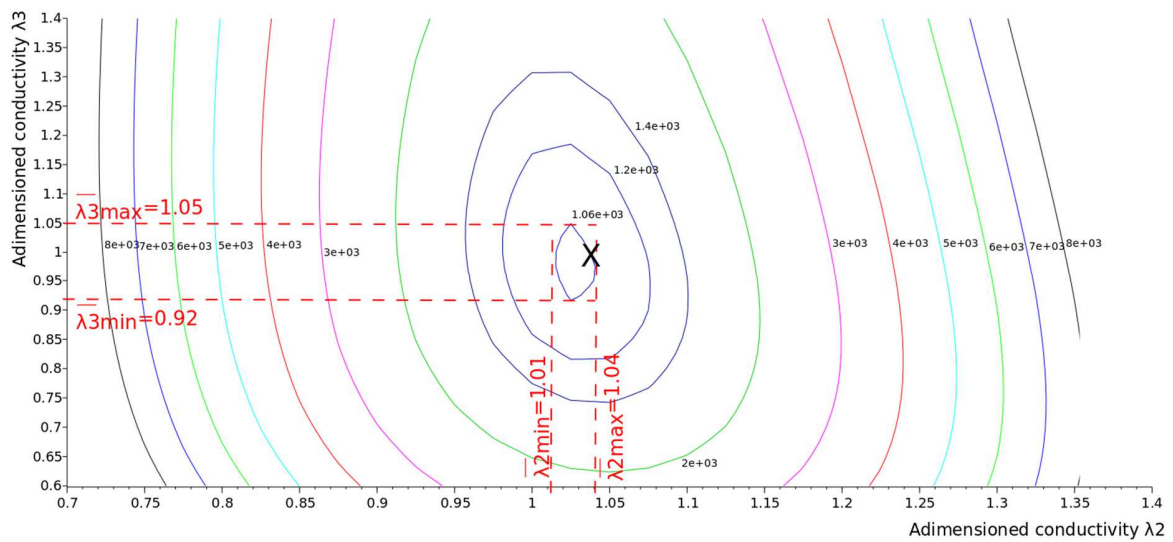


**Fig. 9.** Contour plot of data misfit functional for IWI case #15 considering 12 h time - the black cross denotes the model parameters identified by the IFSTAR deterministic inverse approach.

556

557 **4. Results and discussion**

558 This section presents the main identification results obtained by analyzing the data  
559 provided by Generating Physical Models using the three identification techniques detailed  
560 in section 3 (CERTES, CSTB, IFSTTAR). The simulations are carried out for 24 hours of  
561 thermal solicitation on the wall (step excitation) according to the active approach described  
562 in section 2.2.2. We recall that only the wall typology is known before identification.

563 **4.1 Study of a particular test case: IWI case #15**

564 Let us first discuss the results for IWI case #15 (see table 5 for details). The internal  
565 and external surface temperatures ( $\tilde{T}_{si}$  and  $\tilde{T}_{se}$ ) deduced from the numerical experiment  
566 generated by GPM are shown in figure 10(a) for 24 h of analysis. The temperature  
567 difference between the beginning and the end of the experiment for  $\tilde{T}_{si}$  is approximately  
568 50°C, the active approach proposed therefore leads to a significant heating of the internal  
569 surface of the investigated wall. We can also notice that the external surface temperature  
570  $\tilde{T}_{se}$  is above all sensitive to variations in weather conditions since its increase at the end of  
571 the analysis is due to the increase in incident solar radiation (see Trappes solar radiation  
572 data in figure 4(b)). On the other hand, the heating of the internal surface seems to have a  
573 negligible influence on  $\tilde{T}_{se}$ . Then, figure 10(b) shows the associated residuals at the end of  
574 identification processes. This corresponds to the difference between the “measured”  
575 temperature  $\tilde{T}_{si}$  (computed with GPM) and that estimated after minimization by each of the  
576 identification methods used  $\hat{T}_{si}$ . Overall, the residuals are very close to zero, which shows  
577 the ability of identification methods to accurately reproduce the response of the wall  
578 following the thermal solicitation. The highest residual values in absolute value appear at

579 the start of the thermal excitation ( $t=1$  h). This can be explained by the fact that a constant  
 580 time step is used to solve the direct problem in the identification techniques in order to  
 581 guarantee a good compromise between the accuracy of the identification and the calculation  
 582 time. A shorter time step in the vicinity of the thermal solicitation could make it possible to  
 583 reduce the residuals. It should be noted that the bias appearing at the end of the analysis for  
 584 the IFSTTAR method could be explained by discrepancy principle constraints of the  
 585 corresponding identification method (see section 3.3).

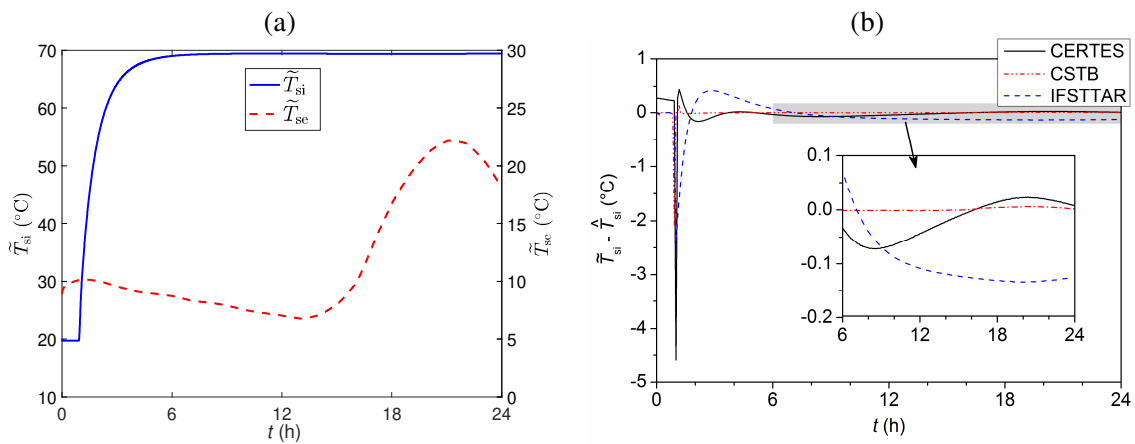


**Fig. 10.** Results for IWI case #15 of the numerical benchmark for 24 hours of analysis:  
 (a) Internal and external surface temperatures generated by GPM according to the observation  
 time, (b) Residuals obtained by each identification method according to the observation time.

586 Let us analyze in figure 11 the evolution of the identified thermal resistance  $\hat{R}$   
 587 according to the observation time for the IWI case #15, the exact thermal resistance  $\tilde{R}$  being  
 588 marked by a horizontal line. We see that the active excitation on the internal wall surface  
 589 and the monitoring of wall surface temperatures has to be conducted at least 8 h with the  
 590 CSTB and IFSTTAR methods in order to properly determine the thermal resistance of this  
 591 IWI case, CERTES method requires 20 h to be accurate. The identifications obtained for  
 592 short analysis times (less than 6 h) lead to an overestimated or under-estimated resistance

593 depending on the method used. We also observe that the identified resistance by CSTB  
 594 method undergoes a variation after 20 h of analysis. In fact the quick temperature rise of the  
 595 external surface temperature due to the increase of the solar radiation at about 20 h (see  
 596 figure 10(a)) disturbs the CSTB identification model. So it seems that the CSTB  
 597 identification method is more sensitive to sudden changes in weather conditions.

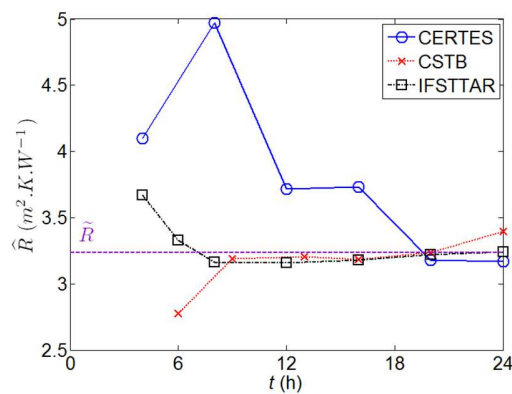


**Fig. 11.** Identified resistances for IWI case #15 according to the observation time.

#### 598 4.2 Main results of the numerical benchmark

599 The thermal resistance  $\hat{R}$  identified by the 3 inverse approaches for IWI and SWS and  
 600 different observation times are summarized in figure 12. The exact value  $\tilde{R}$  of the thermal  
 601 resistance is represented in the  $x$ -axis. For IWI (figures 12(a) and 12(b)), we observe that all  
 602 the inverse approaches are able to identify the resistance within a 20 % precision, on a large  
 603 physical range from about 1  $m^2.K.W^{-1}$  corresponding to bad insulated wall to about 9  
 604  $m^2.K.W^{-1}$ . Nevertheless, few IWI with a thermal resistance between 3 and 4  $m^2.K.W^{-1}$  are  
 605 not properly identified, the reason will be explained using figure 13. The increase of the  
 606 observation time from 12 h to 24 h slightly improves the identification results, especially  
 607 for the IWI cases, the ratios between the identified resistance and the exact resistance

608 getting closer to 1. Indeed, 22 identification results are within a 10 % precision for 12 h and  
 609 25 identification results are within a 10 % precision for 24 h. Also, as shown in figures  
 610 12(c) and 12(d), 1D thermal equations used in CERTES and IFSTTAR inverse techniques  
 611 have to be preferred for the SWS identifications due to modelling error aspects. Indeed, in  
 612 Appendix B we show that the modelling error, caused by the simplification of the 3D  
 613 thermal problem by 1D thermal equations, is higher for SWS than IWI and that it builds up  
 614 over time. Thus, the identified thermal resistances are less accurate for SWS than IWI,  
 615 especially for the CSTB approach using the RC model.

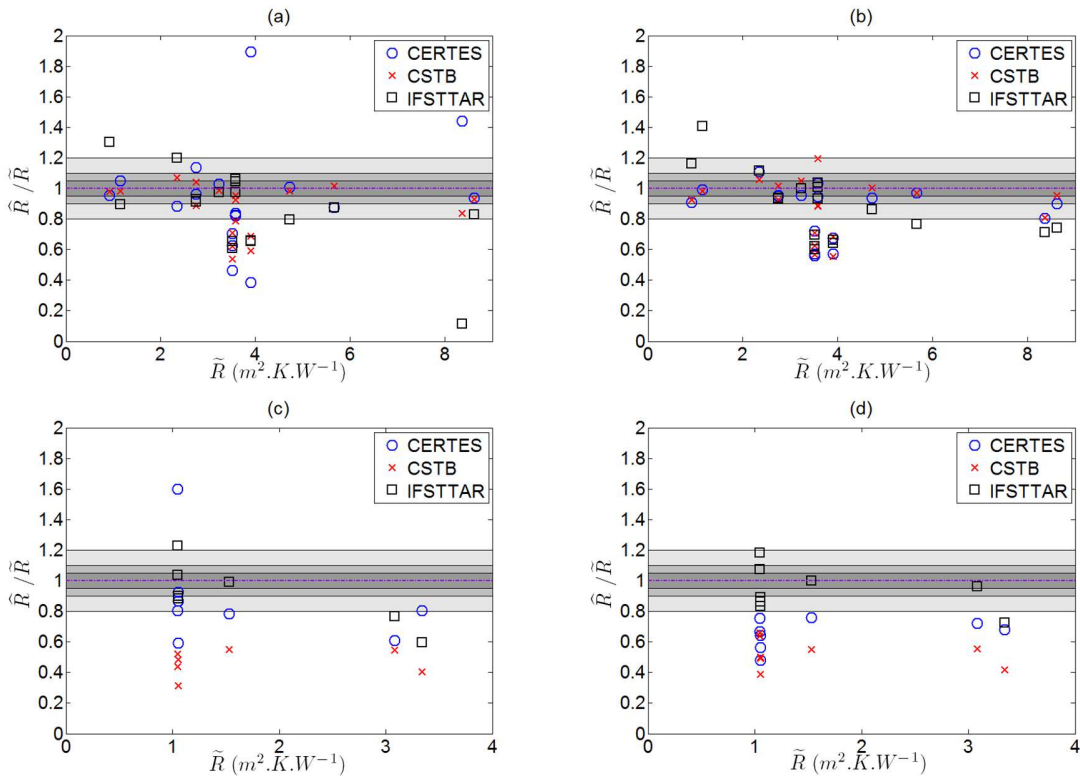


**Fig. 12.** Identified resistances in the numerical benchmark for different walls and different observation times as a function of the exact resistance:  
 (a) IWI-12 h, (b) IWI-24 h, (c) SWS-12 h, (d) SWS-24 h.

616 The identification results for IWI walls are presented according to the total thickness  
 617  $e_{\text{tot}}$  of the wall in figure 13. Even for a large observation time of 24 h, we note that all the

618 inverse techniques fail to identify the thermal resistance when the wall thickness exceeds  
619 45 cm. Figures 12 and 13 show that cases with a large thickness correspond to the cases  
620 with a resistance between 3 and 4 m<sup>2</sup>.K.W<sup>-1</sup>. The bad thermal resistances identified for  
621 these cases can be explained by the presence of a significant lateral heat flow in the wall  
622 which is not taken into account in the simplified models used for the identification leading  
623 to an underestimation of the thermal resistance. The most limiting parameter for the  
624 identification seems to be the wall thickness, more than the thermal resistance, i.e. it is  
625 possible to estimate high thermal resistances with low bias, provided that the thickness of  
626 the wall remains less than about 45 cm. This may be due to the fact that transverse heat  
627 fluxes in the wall, not taken into account in RC and 1D thermal models, cannot be  
628 neglected when the ratio between the wall thickness and the solicitation area dimension is  
629 higher than 0.75. Hence, the identification results can be deteriorated because of the  
630 modelling error coming from transverse heat fluxes.

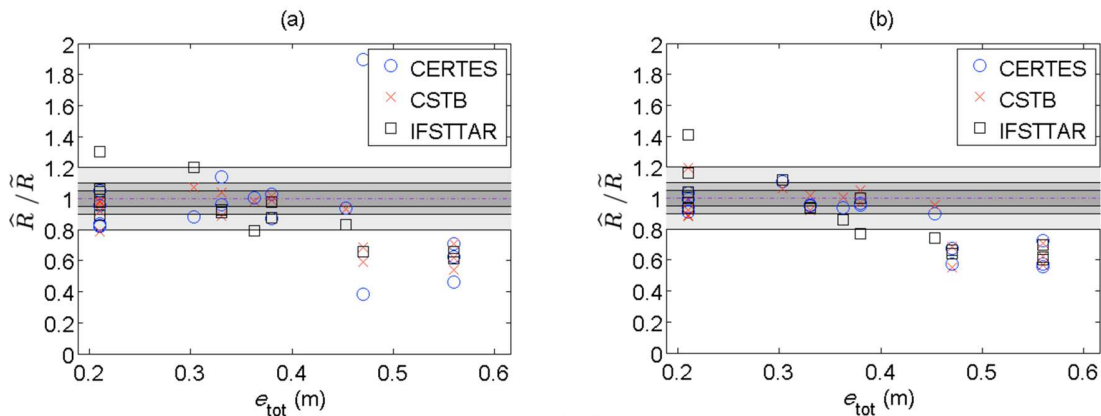


**Fig. 13.** Identified resistances in the numerical benchmark for IWI walls and different observation times as a function of the total thickness: (a) 12 h, (b) 24 h.

631 Figure 14 shows all the identification results of each partner in terms of resistance  
632 and associated uncertainties. We must note that the bias observed for IWI walls of high

633 thicknesses is not detected by the calculation of uncertainty. For both IWI and SWS  
 634 identifications, the thermal resistance confidence intervals derived from IFSTTAR  
 635 approach are too large for operational use except for few IWI cases around  $3 \text{ m}^2 \cdot \text{K} \cdot \text{W}^{-1}$ .

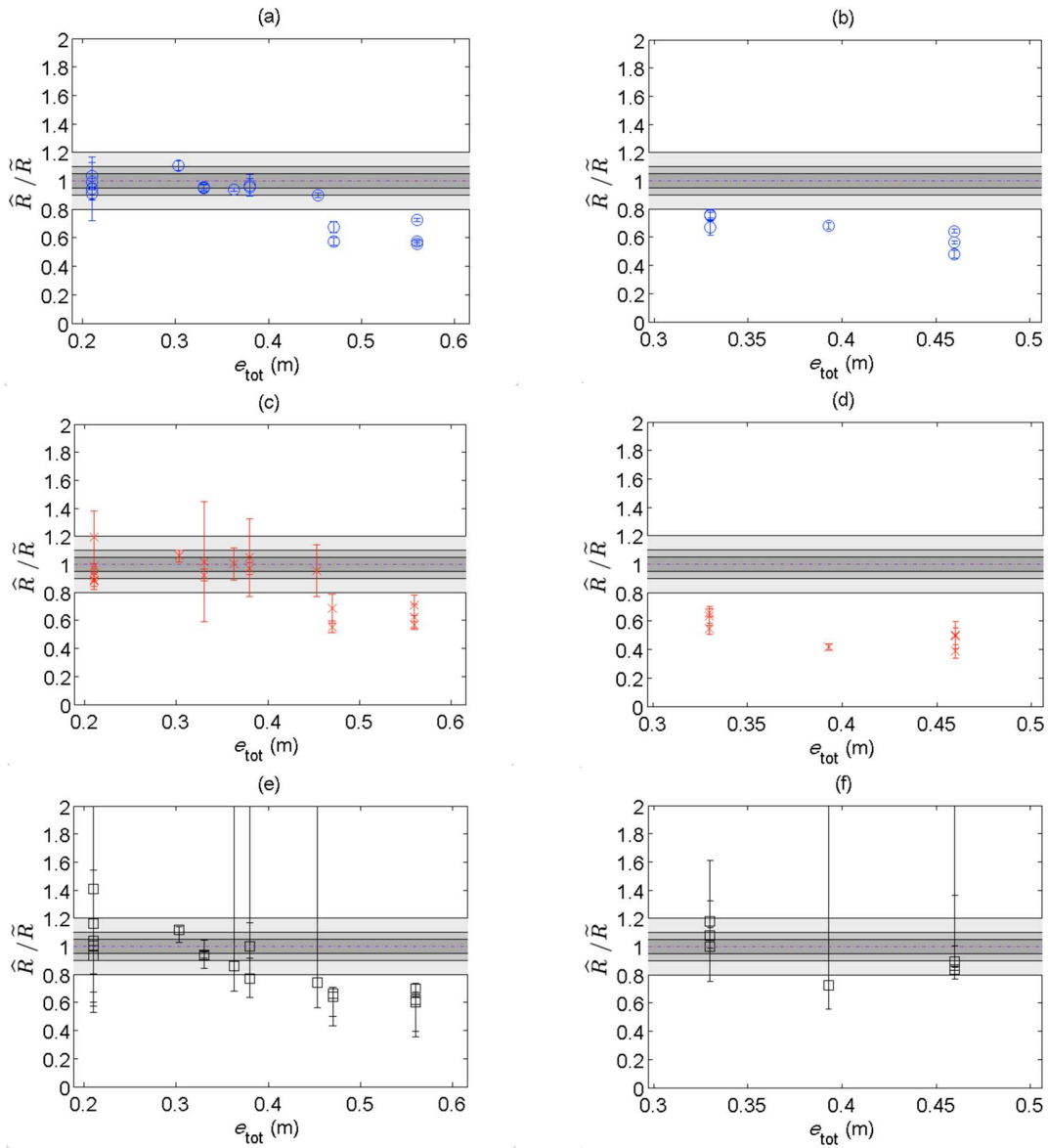


**Fig. 14.** Identified resistances with associated uncertainties for 24 h time observation as a function of the total thickness: (a) CERTES-IWI, (b) CERTES-SWS, (c) CSTB-IWI, (d) CSTB-SWS, (e) IFSTTAR-IWI, (f) IFSTTAR-SWS.

636 As all the lower values of IFSTTAR confidence intervals (except for thick wall cases  
637 discussed previously) are strictly less than the exact thermal resistance, these lower values  
638 can eventually be used as a thermal resistance lower bound. For IWI walls, let us note that  
639 the best identification results are obtained using CSTB technique. Indeed, the identified  
640 resistance ranges for all the studied cases, except the thickest considered walls, are accurate  
641 and include the exact thermal resistance value.

642 As shown in table 5, some IWI (cases 1 to 8) and SWS (cases 19 to 22) cases were  
643 generated by CERTES for two French climate scenarios (H1a/Trappes and H2d/Carpentras  
644 described in section 2.2.3) to study the influence of the weather and of the wall orientation  
645 on the identification process. The couple cases 1-5, 2-6, 3-7, 4-8 (IWI) and 19-21, 20-22  
646 (SWS) refer to the same walls but with different climate scenarios and wall orientations.  
647 We can see in figure 15 that all the identified thermal resistances by the inverse techniques  
648 are almost the same for both climate scenarios and wall orientations. The differences  
649 observed between two different climates and wall orientations in terms of identified  
650 resistance for all the methods are on average 5.5 % and 7.4 % in absolute value,  
651 respectively for the IWI and SWS walls. These small differences show that the heating of  
652 the internal surface induced by the active approach (see figure 10(a)) is sufficient not to be  
653 dependent on weather conditions, time of day or wall orientation. This constitutes an  
654 important practical advantage compared to the passive methods of the literature.

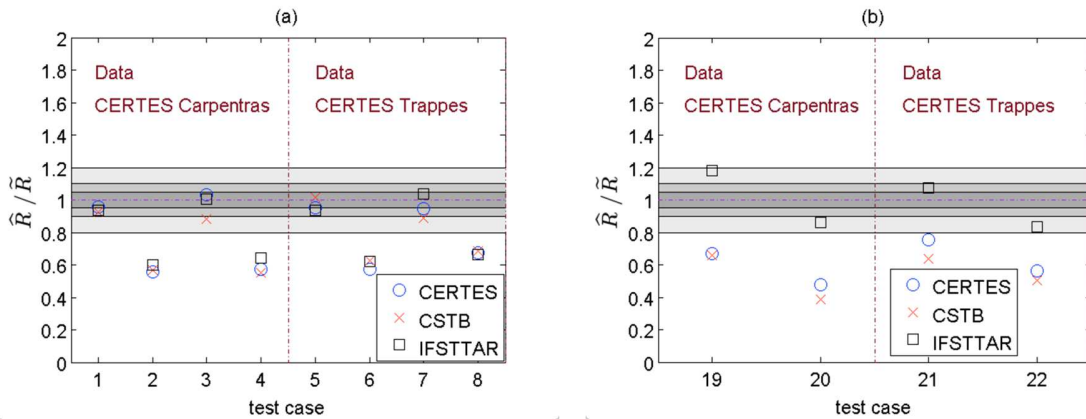


**Fig. 15.** Identified resistances for 24 h time observation and two French climate scenarios and wall orientations: (a) IWI, (b) SWS.

655 Tables 8 and 9 present a summary of the benchmark results. The first one provides  
 656 the numbers of resistance values identified at plus or minus X % of the exact value. It  
 657 shows that the identification technique proposed by CSTB is the most appropriate for  
 658 characterizing IWI while it is preferable to use the IFSTTAR technique for SWS. Thus the  
 659 RC model seems to be suitable for IWI but it is necessary to use more elaborate models (at  
 660 least 1D transient heat equation) for SWS. In addition, we observe that the increase in the  
 661 analysis time from 12 h to 24 h does not significantly improve the identification results.  
 662 Concerning the calculation times involved in this benchmark (see table 9), we can underline  
 663 that the RC model considered in the CSTB approach allows an identification of the thermal  
 664 resistance at a very low computational cost.  
 665

**IWI - 18 test cases**

12 h	CERTES	CSTB	IFSTTAR
±5 %	5	<b>7</b>	3
±10 %	6	<b>10</b>	6
±20 %	<b>12</b>	<b>12</b>	9

24 h	CERTES	CSTB	IFSTTAR
±5 %	<b>6</b>	<b>6</b>	3
±10 %	<b>10</b>	9	6
±20 %	<b>13</b>	<b>13</b>	9

**SWS - 8 test cases**

12 h	CERTES	CSTB	IFSTTAR
±5 %	0	0	<b>2</b>
±10 %	1	0	<b>4</b>
±20 %	4	0	<b>5</b>

24 h	CERTES	CSTB	IFSTTAR
±5 %	0	0	<b>2</b>
±10 %	0	0	<b>3</b>
±20 %	0	0	<b>7</b>

666 **Table 8.** Numbers of resistance values identified by the three identification methods at plus or  
 667 minus X % of the exact value for each wall structure and different observation times  
 668 (yellow color and bold font boxes refer to the identification method(s) that obtain(s) the best score  
 669 at a given percentage).

	CERTES	CSTB	IFSTTAR
<b>12 h</b>	390	20	540
<b>24 h</b>	877	20	720

670 **Table 9.** Average calculation times (in seconds) for the three identification methods and different  
 671 observation times.  
 672

673 **5. Conclusion**

674 The present work consists in a numerical benchmark of identification methods for  
675 estimating the thermal resistance of building walls and is dedicated to the study of internal  
676 wall insulation (IWI) and single-wall structures (SWS). This numerical study is a part of  
677 the ANR RESBATI project whose main objective is to develop a portable measurement  
678 device for evaluating the thermal resistance of opaque building walls on site.  
679 Methodologies exist in scientific literature but do not allow a systematic and rapid  
680 measurement. We propose an active method using a thermal excitation (step excitation) on  
681 the internal surface to create a temperature gradient across the wall and recording a  
682 sequence of temperatures. The originality of the proposed method consists in associating  
683 the active approach with a dynamic regime analysis of the temperature response of the wall  
684 using a robust identification method. The method should provide the value of the thermal  
685 resistance of the wall and its associated uncertainty. This purely numerical work represents  
686 an important task in the current context of improving energy efficiency of existing and new  
687 buildings.

688 The main goal of the numerical benchmark is to evaluate the robustness of different  
689 identification methods, by comparing the bias and uncertainties of each method. First,  
690 Generating Physical Models (thermal quadrupoles, COMSOL and VOLTRA softwares) are  
691 used to generate numerical experiment data as part of a blind process, that is to say  
692 benchmark participants do not know thermal resistances of the walls being studied. Then,  
693 three identification methods use data sets provided by the numerical experiments and the  
694 estimation results are examined. The first one (CERTES) uses thermal quadrupoles and

695 Bayesian estimation. The second method developed by CSTB involves RC networks and  
696 ISABELE method. The last one led by IFSTTAR is based on 1D finite element method and  
697 gradient descent algorithm with adjoint state.

698         Benchmark results show that RC models (0D model) used in the CSTB method are  
699 relevant to identify the thermal resistance of IWI at a very low computational cost. 1D  
700 transient heat equations (CERTES and IFSTTAR) should be preferred to RC models, due  
701 to modelling error, for the identification of SWS thermal resistance. Thanks to the active  
702 thermal strategy, we can expect a relevant *in situ* estimation of the thermal resistance with  
703 an observation time of less than 24 h. This numerical benchmark also shows that the  
704 meteorological conditions and the wall orientation do not impact the results of the three  
705 studied identification processes. This demonstrates the flexibility of using the active  
706 approach.

707         However, it appears that estimating the wall thermal resistance becomes difficult  
708 when the ratio between the wall thickness and the solicitation area dimension is higher than  
709 0.75. This can be explained by significant transverse heat fluxes in the wall, the estimation  
710 results are in that case deteriorated due to an excessive modelling error. To tackle the issue  
711 of transverse heat flux, 2D axisymmetric thermal equations can be considered to improve  
712 the thermal resistance identification results, notably for SWS. A circular shape of the  
713 excitation area would be used instead of the square shape considered in the article which is  
714 more convenient for the experimental design. To drastically reduce the computation time to  
715 solve the 2D thermal equations and thus getting a fast thermal resistance identification  
716 process, we propose to use model order reduction techniques like the “Proper Generalized  
717 Decomposition” [50,51].

718 Other types of walls (External Thermal Insulation Composite System, wood frame  
719 wall) will be investigated in this numerical approach. After this numerical benchmark step,  
720 experiments on IWI and wood frame walls with sensor outputs will be conducted to test the  
721 robustness of the identification methods in real conditions, first under controlled laboratory  
722 conditions then *in situ*.

723

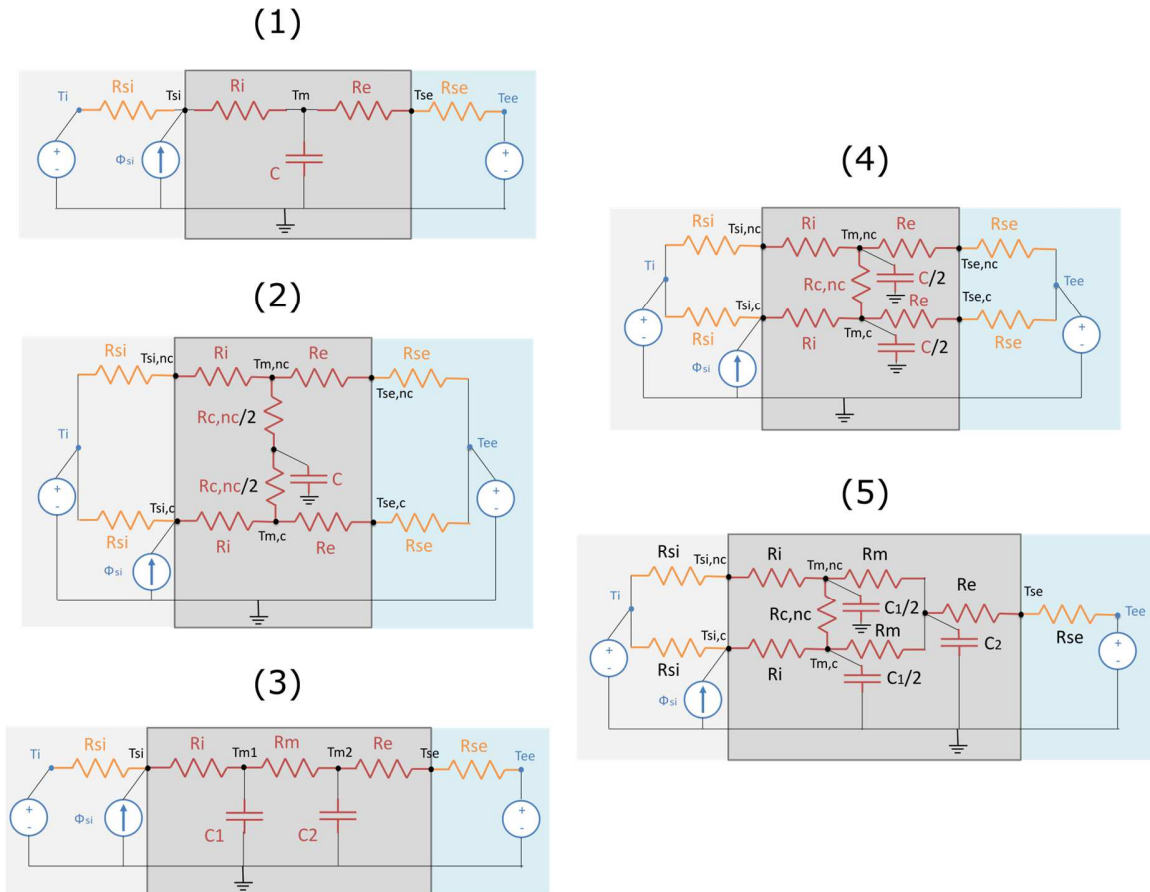
#### 724 **Acknowledgements**

725 This work was supported by the National Research French Agency (ANR) [Project  
726 ID: ANR-16-CE22-0010]. We also want to thank Philippe Lévèque, engineer at IFSTTAR,  
727 for his help in the development of a Python script to supervise massive computations in 3D  
728 and in 1D with the finite element software CESAR-LCPC in view of evaluating the  
729 modelling error.

730

731 **Appendix A: RC structures of the CSTB method and related equations**

732 Figure A.1 presents all RC structures used in the CSTB method to evaluate the  
 733 thermal resistance of a wall under dynamic conditions [52].



734

735 **Fig. A.1.** Illustration of proposed RC structures for the simplified thermal dynamics of the wall  
 736 (CSTB method).

737 Parameters in blue correspond to the boundary conditions (measured temperatures,  
 738 heat flows). Resistances in yellow refer to known resistances. Capacitances and resistances  
 739 in red correspond to the unknown parameters to optimize. It is important to note that the  
 740 uncertainty on these boundary conditions (temperatures, heat flows, known resistances)

741 should be considered under real experimental conditions. Nevertheless, it can be neglected  
 742 under simulation conditions.

743 - **Model 1:**

744 Figure A.1(1) presents the simplest RC structure. The corresponding single state  
 745 equation is:

$$746 \quad C \frac{dT_m}{dt} = (R_e + R_{se})^{-1}(T_{ee} - T_m) + (R_i + R_{si})^{-1}(T_i - T_m) + \frac{R_{si}\Phi_{si}}{R_i + R_{si}} + \sigma_m \frac{d\omega_m}{dt} \quad (\text{A.1})$$

747 The observation equation is:

$$748 \quad T_{si} = \frac{R_i T_i + R_{si} T_m + R_i R_{si} \Phi_{si}}{R_i + R_{si}} + \varepsilon(\sigma_{T_{si}, mes}) \quad (\text{A.2})$$

749 The corresponding  $R$ -value and uncertainty are calculated by the following equations:

$$750 \quad \hat{R}_{wall} = \hat{R}_i + \hat{R}_e \quad (\text{A.3})$$

$$751 \quad \hat{\sigma}_{R_{wall}} = \sqrt{J \text{cov}(\hat{R}_i, \hat{R}_e) J^T} = \sqrt{\text{cov}(\hat{R}_i, \hat{R}_e)} \quad \text{as } J = (1 \quad 1) \quad (\text{A.4})$$

752 - **Model 2:**

753 Figure A.1(2) presents another RC structure taking into account the lateral heat  
 754 transfer within the inner face of the wall. The corresponding single state equation is:

$$755 \quad C \frac{dT_m}{dt} = \frac{4(T_{ee} - T_m)}{2R_e + 2R_{se} + R_{cnc} + \frac{(R_e + R_{se})R_{cnc}}{R_i + R_{si}}} + \frac{4(T_i - T_m) + 2R_{si}\Phi_{si}}{2R_i + 2R_{si} + R_{cnc} + \frac{(R_i + R_{si})R_{cnc}}{R_e + R_{se}}} + \sigma_m \frac{d\omega_m}{dt} \quad (\text{A.5})$$

757 The observation equation is:

$$758 \quad T_{si,c} = \frac{R_i T_i + R_{si} T_{m,c} + R_i R_{si} \Phi_{si}}{R_i + R_{si}} + \varepsilon(\sigma_{T_{si}, mes}) \quad (\text{A.6})$$

759 with:

$$760 \quad T_{m,c} = \frac{2(R_e + R_{se})(R_i + R_{si})T_m + R_{cnc}(R_i + R_{si})T_{ee} + R_{cnc}(R_e + R_{se})T_i + R_{cnc}(R_i + R_{si})(R_e + R_{se})\Phi_{si}}{2(R_e + R_{se})(R_i + R_{si}) + R_{cnc}(R_i + R_{si}) + R_{cnc}(R_e + R_{se})} \quad (\text{A.7})$$

762 The corresponding  $R$ -value and uncertainty are calculated the same way as in Model 1.

763 - **Model 3:**

764 Figure A.1(3) presents a 2-order RC structure. The corresponding state equations are:

$$765 \quad C_1 \frac{dT_{m1}}{dt} = R_m^{-1}(T_{m2} - T_{m1}) + (R_i + R_{si})^{-1}(T_i - T_m) + \frac{R_{si}\Phi_{si}}{R_i + R_{si}} + \sigma_{m1} \frac{d\omega_{m1}}{dt}$$

766 (A.8)

$$767 \quad C_2 \frac{dT_{m2}}{dt} = R_m^{-1}(T_{m1} - T_{m2}) + (R_e + R_{se})^{-1}(T_{ee} - T_{m2}) + \sigma_{m2} \frac{d\omega_{m2}}{dt}$$

768 (A.9)

769 The observation equation is:

$$770 \quad T_{si} = \frac{R_i T_i + R_{si} T_{m1} + R_i R_{si} \Phi_{si}}{R_i + R_{si}} + \varepsilon(\sigma_{T_{si}, mes}) \quad (A.10)$$

771 The corresponding  $R$ -value and uncertainty are calculated by the following equations:

$$772 \quad \hat{R}_{wall} = \hat{R}_i + \hat{R}_m + \hat{R}_e \quad (A.11)$$

$$773 \quad \hat{\sigma}_{R_{wall}} = \sqrt{Jcov(\hat{R}_i, \hat{R}_m, \hat{R}_e)J^T} = \sqrt{cov(\hat{R}_i, \hat{R}_m, \hat{R}_e)} \text{ as } J = (1 \quad 1 \quad 1) \quad (A.12)$$

774 - **Model 4:**

775 Figure A.1(4) presents another RC structure taking into account the lateral heat  
776 transfer within the inner face of the wall. The corresponding state equations are:

$$777 \quad \frac{C}{2} \frac{dT_{m,c}}{dt} = R_{c,nc}^{-1}(T_{m,nc} - T_{m,c}) + (R_e + R_{se})^{-1}(T_{ee} - T_{m,c}) + (R_i + R_{si})^{-1}(T_i - T_{m,c}) + \frac{R_{si}\Phi_{si}}{R_i + R_{si}} + \sigma_{m,c} \frac{d\omega_{m,c}}{dt}$$

778 (A.13)

$$780 \quad \frac{C}{2} \frac{dT_{m,nc}}{dt} = R_{c,nc}^{-1}(T_{m,c} - T_{m,nc}) + (R_e + R_{se})^{-1}(T_{ee} - T_{m,nc}) + (R_i + R_{si})^{-1}(T_i - T_{m,nc}) + \sigma_{m,nc} \frac{d\omega_{m,nc}}{dt}$$

781 (A.14)

782 The observation equation is:

$$783 \quad T_{si,c} = \frac{R_i T_i + R_{si} T_{m,c} + R_i R_{si} \Phi_{si}}{R_i + R_{si}} + \varepsilon(\sigma_{T_{si}, mes}) \quad (A.15)$$

784 The corresponding  $R$ -value and uncertainty are calculated the same way as in Model 1.

785

786 - **Model 5:**

787 Figure A.1(5) presents the most complex RC structure taking into account the lateral  
788 heat transfer within the inner face of the wall. The corresponding 3 state equations are:

789 
$$\frac{C_1}{2} \frac{dT_{m,c}}{dt} = R_{c,nc}^{-1}(T_{m,nc} - T_{m,c}) + R_m^{-1}(T_{m2} - T_{m,c}) + (R_i + R_{si})^{-1}(T_i - T_{m,c}) + \frac{R_{si}\Phi_{si}}{R_i + R_{si}} + \sigma_{m,c} \frac{d\omega_{m,c}}{dt}$$
  
790 (A.16)  
791

792 
$$\frac{C_1}{2} \frac{dT_{m,nc}}{dt} = R_{c,nc}^{-1}(T_{m,c} - T_{m,nc}) + R_m^{-1}(T_{m2} - T_{m,nc}) + (R_i + R_{si})^{-1}(T_i - T_{m,nc}) + \sigma_{m,nc} \frac{d\omega_{m,nc}}{dt}$$
  
793 (A.17)  
794

795 
$$C_2 \frac{dT_{m2}}{dt} = R_m^{-1}(T_{m,c} - T_{m2}) + R_m^{-1}(T_{m,nc} - T_{m2}) + (R_e + R_{se})^{-1}(T_{ee} - T_{m2}) + \sigma_{m2} \frac{d\omega_{m2}}{dt}$$
  
796 (A.18)

797 The observation equation is:

798 
$$T_{si,c} = \frac{R_i T_i + R_{si} T_{m,c} + R_i R_{si} \Phi_{si}}{R_i + R_{si}} + \varepsilon(\sigma_{Tsi,mes})$$
 (A.19)

799 The corresponding R-value and uncertainty are calculated the same way as in Model 3.

800

## 801 **Appendix B: Estimation of modelling error (IFSTTAR method)**

802 As described in section 3.3, IFSTTAR inverse procedure takes into account the  
803 modelling error due to the simplification of the three-dimensional (3D) thermal problem to  
804 one-dimensional (1D) transient heat equations. To estimate the modelling error on the  
805 temperatures at the internal and external wall surfaces, about 500 sets of parameters have  
806 been randomly drawn in agreement with the variation range of the considered wall  
807 typology given in table 1. For each set of parameters (corresponding to 4 layer thicknesses,  
808 4 conductivities and 4 thermal capacities for a IWI wall), the 3D wall thermal problem is  
809 solved using standard finite methods and Implicit Euler time integration scheme with the  
810 software CESAR-LCPC [53] and the computed temperatures  $T3d_i(t)$  and  $T3d_e(t)$  at the  
811 inside and the outside faces of the wall are stored. Likewise, the numerical temperatures  
812  $T1d_i(t)$  and  $T1d_e(t)$  at both faces of the wall are obtained solving a 1D transient heat  
813 problem. From that, we can evaluate on a time interval  $[0 ; t_f]$  the cumulative modelling  
814 error  $J_{ME}$  and the indicative temperature modelling error  $T_{ME}$  defined by:

$$815 \quad J_{ME} = \frac{1}{2} \int_{t=0}^{t=t_f} ((T3d_i - T1d_i)^2 + (T3d_e - T1d_e)^2) dt \quad (B.1)$$

$$816 \quad T_{ME} = \sqrt{\frac{J_{ME}}{t_f}} \quad (B.2)$$

817 The cumulative and the temperature modelling errors are represented in figures B.1  
818 and B.2 for the IWI wall and the single wall respectively for the time interval  $[0 ; t_f=12 \text{ h}]$ .  
819 A modelling error threshold is shown in red. It is defined such that 80 % of the IWI walls  
820 (resp. the single walls) have a cumulative modelling error less than this threshold. In  
821 practice, the modelling error threshold is used in the IFSTTAR inverse technique. We  
822 observe that the modelling error is higher for the single wall than the IWI wall. Indeed, on a

823 12 h time interval, 80 % of the single walls have a temperature modelling error less than  
 824 0.2°C, whereas it is less than 0.15°C for the IWI walls.

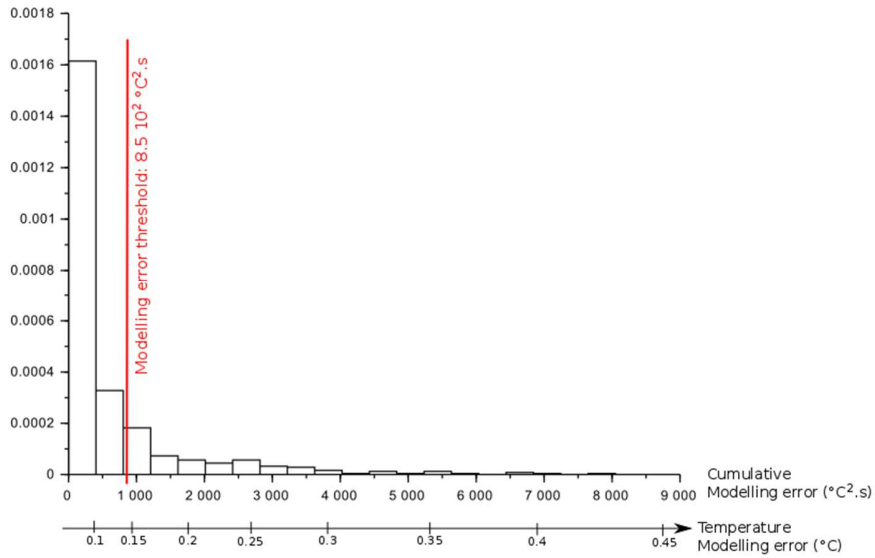


**Fig. B.1.** Distribution of cumulative and temperature modelling errors for IWI wall for a 12 h time interval, computed from about 500 numerical simulations.

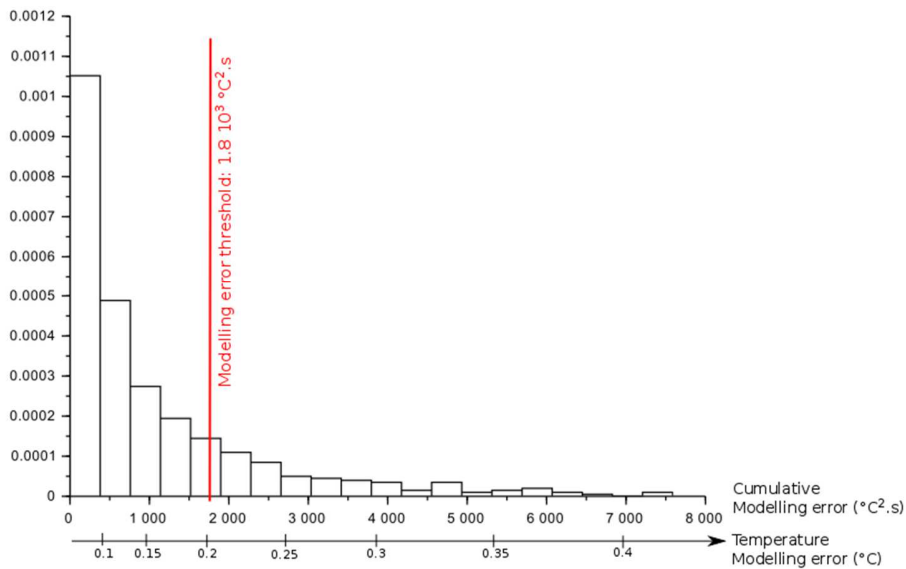


**Fig. B.2.** Distribution of cumulative and temperature modelling errors of Single wall for a 12 h time interval, computed from about 500 numerical simulations.

825 Finally, we summarize in tables B.1 and B.2 for IWI and single walls the modelling

826 error threshold and the associated temperature modelling error for several time intervals  
827 (also beyond 24 h). For IWI and single walls, we note an increase of the modelling error  
828 when considering bigger time intervals. Tables B.1 and B.2 also show that the modelling  
829 error is higher for the single wall than the IWI wall. For a 72 h time interval, the  
830 temperature modelling error of the single wall is four times bigger than the one of the IWI  
831 wall. To conclude, we highlight that the inverse procedure may lead to inaccurate  
832 identification results when considering a large time interval as 72 h and/or single wall  
833 typology due to excessive modelling error.

	12 h	24 h	48 h	72 h
Modelling error threshold ( $^{\circ}\text{C}^2.\text{s}$ )	$8.5 \cdot 10^2$	$4.2 \cdot 10^3$	$1.5 \cdot 10^4$	$2.8 \cdot 10^4$
Temperature modelling error ( $^{\circ}\text{C}$ )	0.14	0.22	0.29	0.33

834 **Table B.1.** Modelling error threshold and associated temperature modelling error for IWI for  
835 several time intervals.

	12 h	24 h	48 h	72 h
Modelling error threshold ( $^{\circ}\text{C}^2.\text{s}$ )	$1.8 \cdot 10^3$	$2.9 \cdot 10^4$	$2.1 \cdot 10^5$	$4.9 \cdot 10^5$
Temperature modelling error ( $^{\circ}\text{C}$ )	0.2	0.58	1.1	1.37

836 **Table B.2.** Modelling error threshold and associated temperature modelling error for SWS for  
837 several time intervals.

838

839 **References**

- 840 [1] Réglementation Thermique RT 2012, Ed. Centre Scientifique et Technique du  
841 Bâtiment, 2012 (in French).
- 842 [2] PERFORMER Project, "Portable, Exhaustive, Reliable, Flexible and Optimized  
843 approach to Monitoring and Evaluation of building energy performance", [http://performer-](http://performer-project.eu)  
844 [project.eu](http://performer-project.eu), 2014.
- 845 [3] S. Roels, "The IEA EBC Annex 58 - project on 'reliable building energy performance  
846 characterisation based on full scale dynamic measurements'", IEA Annex 58 Seminar -  
847 Real building energy performance assessment, Gent, 2014.
- 848 [4] J. Berger, S. Tasca-Guernouti, M. Humbert, "Experimental method to determine the  
849 energy envelope performance of building", 10<sup>th</sup> International Conference for Enhanced  
850 Building Operations, Kuwait, 2010.
- 851 [5] P. Bacher, H. Madsen, "Identifying suitable models for the heat dynamics of buildings",  
852 *Energy and Buildings*, 43(7), p. 1511-1522, 2011.
- 853 [6] S. Thébault, R. Bouchié, "Refinement of the ISABELE method regarding uncertainty  
854 quantification and thermal dynamics modelling", *Energy and Buildings*, 178, p. 182-205,  
855 2018.
- 856 [7] F. Alzetto, J. Meulemans, G. Pandraud, D. Roux, "A perturbation method to estimate  
857 building thermal performance", *C. R. Chimie*, 21, p. 938-942, 2018.
- 858 [8] N. Soares, C. Martins, M. Gonçalves, P. Santos, L. S. da Silva, J. J. Costa, "Laboratory  
859 and *in-situ* non-destructive methods to evaluate the thermal transmittance and behavior of  
860 walls, windows, and construction elements with innovative materials: A review", *Energy*  
861 *and Buildings*, 182, p. 88-110, 2019.
- 862 [9] ISO 8990:1994, "Thermal insulation - Determination of steady-state thermal  
863 transmission properties - Calibrated and guarded hot box", ISO Standard, 1994.
- 864 [10] ISO 9869-1:2014, "Thermal insulation - Building elements - In-situ measurement of  
865 thermal resistance and thermal transmittance - Part 1: Heat flow meter method", ISO  
866 Standard, 2014.
- 867 [11] A. Rasooli, L. Itard, C. I. Ferreira, "A response factor-based method for the rapid *in-*  
868 *situ* determination of wall's thermal resistance in existing buildings", *Energy and Buildings*,  
869 119, p. 51-61, 2016.
- 870 [12] G. P. Mitalas, D. G. Stephenson, "Room thermal response factors", *ASHRAE*  
871 *Transactions*, 73(1), p.1-10, 1967.
- 872 [13] A. Rasooli, L. Itard, "In-situ rapid determination of walls' thermal conductivity,  
873 volumetric heat capacity, and thermal resistance, using response factors", *Applied Energy*,  
874 253, 113539, 2019.
- 875 [14] A. Nowoświat, J. Skrzypczyk, P. Krause, T. Steidl, A. Winkler-Skalna, "Estimation of  
876 thermal transmittance based on temperature measurements with the application of  
877 perturbation numbers", *Heat and Mass Transfer*, 54, p. 1477-1489, 2018.
- 878 [15] I. Naveros, M. J. Jiménez, M. R. Heras, "Analysis of capabilities and limitations of the  
879 regression method based in averages, applied to the estimation of the  $U$  value of building  
880 component tested in Mediterranean weather", *Energy and Buildings*, 55, p. 854-872, 2012.

- 881 [16] I. Danielski, M. Fröling, "Diagnosis of buildings' thermal performance - a quantitative  
882 method using thermography under non-steady state heat flow", *Energy Procedia*, 83, p.  
883 320-329, 2015.
- 884 [17] R. Albatici, A. M. Tonelli, "Infrared thermovision technique for the assessment of  
885 thermal transmittance value of opaque building elements on site", *Energy and Buildings*,  
886 42, p. 2177-2183, 2010.
- 887 [18] R. Albatici, A. M. Tonelli, M. Chiogna, "A comprehensive experimental approach for  
888 the validation of quantitative infrared thermography in the evaluation of building thermal  
889 transmittance", *Applied Energy*, 141, p. 218-228, 2015.
- 890 [19] I. Nardi, S. Sfarra, D. Ambrosini, "Quantitative thermography for the estimation of the  
891 U-value: state of the art and a case study", *Journal of Physics: Conference Series*, 547,  
892 2014.
- 893 [20] P. A. Fokaidis, S. A. Kalogirou, "Application of infrared thermography for the  
894 determination of the overall heat transfer coefficient (*U*-Value) in building envelopes",  
895 *Applied Energy*, 88, p. 4358-4365, 2011.
- 896 [21] B. Tejedor, M. Casals, M. Gangoellés, X. Roca, "Quantitative internal infrared  
897 thermography for determining in-situ thermal behaviour of façades", *Energy and Buildings*,  
898 151, p. 187-197, 2017.
- 899 [22] B. Tejedor, M. Casals, M. Gangoellés, "Assessing the influence of operating conditions  
900 and thermophysical properties on the accuracy of in-situ measured U-values using  
901 quantitative internal infrared thermography", *Energy and Buildings*, 171, p. 64-75, 2018.
- 902 [23] S. Kato, K. Kuroki, S. Hagihara, "Method of in-situ measurement of thermal insulation  
903 performance of building elements using infrared camera", 6<sup>th</sup> IAQVEC, Sendai, Japan,  
904 2007.
- 905 [24] ISO 9869-2:2018, "Thermal insulation - Building elements - In-situ measurement of  
906 thermal resistance and thermal transmittance - Part 2: Infrared method for frame structure  
907 dwelling", ISO Standard, 2018.
- 908 [25] E. Sassine, "A practical method for in-situ thermal characterization of walls", *Case  
909 Studies in Thermal Engineering*, 8, p. 84-93, 2016.
- 910 [26] P. Lagonotte, Y. Bertin, J.-B. Saulnier, "Analyse de la qualité de modèles nodaux  
911 réduits à l'aide de la méthode des quadripôles", *International Journal of Thermal Sciences*,  
912 38(1), p. 51-65, 1999.
- 913 [27] K. Chaffar, A. Chauchois, D. Defer, L. Zalewski, "Thermal characterization of  
914 homogeneous walls using inverse method", *Energy and Buildings*, 78, p. 248-255, 2014.
- 915 [28] T. Wu, "Formalisme des impédances thermiques généralisées: application à la  
916 caractérisation thermique de parois de bâtiments", Ph.D. Thesis, Université d'Artois, 2011  
917 (in French).
- 918 [29] P. Biddulph, V. Gori, C. A. Elwell, C. Scott, C. Rye, R. Lowe, T. Oreszczyn,  
919 "Inferring the thermal resistance and effective thermal mass of a wall using frequent  
920 temperature and heat flux measurements", *Energy and Buildings*, 78, p. 10-16, 2014.
- 921 [30] L. De Simon, M. Iglesias, B. Jones, C. Wood, "Quantifying uncertainty in  
922 thermophysical properties of walls by means of Bayesian inversion", *Energy and Buildings*,  
923 177, p. 220-245, 2018.

924 [31] Z. Petojević, R. Gospavić, G. Todorović, "Estimation of thermal impulse response of a  
925 multi-layer building wall through in-situ experimental measurements in a dynamic regime  
926 with applications", *Applied Energy*, 228, p. 468-486, 2018.

927 [32] M. Larbi Youcef, V. Feuillet, L. Ibos, Y. Candau, P. Balcon, A. Filloux, "Quantitative  
928 diagnosis of insulated building walls of restored old constructions using active infrared  
929 thermography", *QIRT Journal*, 8, p. 65-87, 2011.

930 [33] Règles Th-Bât, Fascicule Matériaux, [www.rt-batiment.fr/IMG/pdf/2-](http://www.rt-batiment.fr/IMG/pdf/2-fascicule_materiaux.pdf)  
931 [fascicule\\_materiaux.pdf](http://www.rt-batiment.fr/IMG/pdf/2-fascicule_materiaux.pdf), 2017 (in French).

932 [34] Données météorologiques de la RT 2012, Ed. Centre Scientifique et Technique du  
933 Bâtiment, [www.rt-batiment.fr/les-donnees-meteorologiques-rt-2012-a14.html](http://www.rt-batiment.fr/les-donnees-meteorologiques-rt-2012-a14.html), 2012 (in  
934 French).

935 [35] French energetic regulation, "Arrêté du 30 avril 2013 portant approbation de la  
936 méthode de calcul Th-BCE 2012 prévue aux articles 4, 5 et 6 de l'arrêté du 26 octobre 2010  
937 relatif aux caractéristiques thermiques et aux exigences de performance énergétique des  
938 bâtiments nouveaux et des parties nouvelles de bâtiments", §5.2, p. 41-47, 2013.

939 [36] ISO 6946:2017, "Building components and building elements - Thermal resistance and  
940 thermal transmittance - Calculation methods", ISO Standard, 2017.

941 [37] D. Maillet, S. André, J.-C. Batsale, A. Degiovanni, C. Moyne, "Thermal Quadrupoles,  
942 Solving the heat equation through integral transforms", Ed. Wiley, 2000.

943 [38] F. R. de Hoog, J. H. Knight, A. N. Stokes, "An Improved Method for Numerical  
944 Inversion of Laplace Transforms", *SIAM Journal on Scientific and Statistical Computing*,  
945 3, p. 357-366, 1982.

946 [39] VOLTRA v8.0w - Detailed simulation of transient thermal effects 3D building  
947 elements, [www.physibel.be/en/products/voltra](http://www.physibel.be/en/products/voltra), Physibel, Ghent, Belgium.

948 [40] P. Standaert, P. Houthuys, J. Langmans, W. Parys, "Detailed experimental validation  
949 of a transient 3D thermal model with solar processor", 13<sup>th</sup> Conference on Advanced  
950 Building Skins, Bern, Switzerland, 2018.

951 [41] M. K. Kumaran, "The IEA Annex 24 - Heat, air and moisture transfer in insulated  
952 envelope parts", Volume 3, Task 3: Material Properties, Final report, Leuven: Laboratorium  
953 Bouwfysica, Departement Burgerlijke Bouwkunde, 1996.

954 [42] COMSOL Multiphysics v.5.3, [www.comsol.com](http://www.comsol.com), COMSOL AB, Stockholm, Sweden.

955 [43] N. Metropolis, S. Ulam, "The Monte Carlo method", *Journal of the American*  
956 *Statistical Association*, 44(247), p. 335-341, 1949.

957 [44] W.K. Hastings, "Monte Carlo Sampling Methods Using Markov Chains and Their  
958 Applications", *Biometrika*, 57(1), p. 97-109, 1970.

959 [45] M. Vihola, "Robust adaptive Metropolis algorithm with coerced acceptance rate",  
960 *Statistics and Computing*, 22, p. 997-1008, 2012.

961 [46] CTSM-R: Continuous-Time Stochastic Modelling for R, [www.ctsm.info](http://www.ctsm.info).

962 [47] N.R. Kristensen, H. Madsen, "Continuous-time stochastic modelling 2.3: mathematics  
963 guide", Technical Report, Technical University of Denmark, 2003.

964 [48] A. Tikhonov, Y. Arsenin, "Solutions to ill-posed problems", Ed. Wiley, 1977.

965 [49] H. W. Engl, M. Hanke, A. Neubauer, "Regularization of inverse problems", Kluwer  
966 Academic Publishers, 2000.

- 967 [50] A. Nouy, "A priori model reduction through Proper Generalized Decomposition for  
968 solving time-dependent partial differential equations", *Computer Methods in Applied*  
969 *Mechanics and Engineering*, 199, p. 1603-1626, 2010.
- 970 [51] F. Chinesta, P. Ladeveze, E. Cueto, "A Short Review on Model Order Reduction  
971 Based on Proper Generalized Decomposition", *Archives of Computational Methods in*  
972 *Engineering*, 18, p. 395-404, 2011.
- 973 [52] S. Thébault, "Contribution à l'évaluation in situ des performances d'isolation  
974 thermique de l'enveloppe des bâtiments", Ph. D. Thesis, Université de Lyon, 2017 (in  
975 French).
- 976 [53] P. Humbert, "Cesar-LCPC, un code général de calcul par éléments finis", *Bulletin de*  
977 *liaison des Laboratoires des Ponts et Chaussées*, 160, 1989 (in French).